



# Investigation of smectite hydration properties by modeling experimental X-ray diffraction patterns. Part I. Montmorillonite hydration properties.

Eric Ferrage, Bruno Lanson, Boris A. Sakharov, Victor A. Drits

## ► To cite this version:

Eric Ferrage, Bruno Lanson, Boris A. Sakharov, Victor A. Drits. Investigation of smectite hydration properties by modeling experimental X-ray diffraction patterns. Part I. Montmorillonite hydration properties.. American Mineralogist, Mineralogical Society of America, 2005, 90, pp.1358-1374. <hal-00105756>

**HAL Id: hal-00105756**

**<https://hal.archives-ouvertes.fr/hal-00105756>**

Submitted on 12 Oct 2006

**HAL** is a multi-disciplinary open access archive for the deposit and dissemination of scientific research documents, whether they are published or not. The documents may come from teaching and research institutions in France or abroad, or from public or private research centers.

L'archive ouverte pluridisciplinaire **HAL**, est destinée au dépôt et à la diffusion de documents scientifiques de niveau recherche, publiés ou non, émanant des établissements d'enseignement et de recherche français ou étrangers, des laboratoires publics ou privés.

1 Investigation of smectite hydration properties by modeling experimental X-ray  
2 diffraction patterns. Part I. Montmorillonite hydration properties

3 **Revision 1**

4 Eric Ferrage<sup>1,2</sup>, Bruno Lanson<sup>1</sup>, Boris A. Sakharov<sup>3</sup>, and Victor A. Drits<sup>3</sup>

5

6 <sup>1</sup> Environmental Geochemistry Group, LGIT – Maison des Géosciences, Joseph Fourier  
7 University – CNRS, BP53, 38041 Grenoble cedex 9, France

8 <sup>2</sup> ANDRA, Parc de la Croix Blanche, 1-7 rue Jean Monnet, 92298 Châtenay-Malabry  
9 cedex, France

10 <sup>3</sup> Geological Institute, Russian Academy of Sciences, 7 Pyzhevsky street, 109017  
11 Moscow, Russia

12

13 Corresponding author: Eric.Ferrage@obs.ujf-grenoble.fr

14

15

**ABSTRACT**

16

17 Hydration of the <1 μm size fraction of SWy-1 source clay (low-charge  
18 montmorillonite) was studied by modeling of X-ray diffraction (XRD) patterns recorded  
19 under controlled relative humidity (RH) conditions on Li-, Na-, K-, Mg-, Ca-, and Sr-  
20 saturated specimens. The quantitative description of smectite hydration, based on the relative  
21 proportions of different layer types derived from the fitting of experimental XRD patterns,  
22 was consistent with previous reports of smectite hydration. However, the coexistence of  
23 smectite layer types exhibiting contrasting hydration states was systematically observed, and  
24 heterogeneity rather than homogeneity seems to be the rule for smectite hydration. This  
25 heterogeneity can be characterized qualitatively using the standard deviation of the departure

26 from rationality of the  $00\ell$  reflection series ( $\xi$ ), which is systematically larger than 0.4 Å  
27 when the prevailing layer type accounts for ~70% or less of the total layers (~25 of XRD  
28 patterns examined). In addition, hydration heterogeneities are not randomly distributed within  
29 smectite crystallites, and models describing these complex structures involve two distinct  
30 contributions, each containing different layer types that are randomly interstratified. As a  
31 result, the different layer types are partially segregated in the sample. However, these two  
32 contributions do not imply the actual presence of two populations of particles in the sample.

33 XRD profile modeling has allowed also the refinement of structural parameters, such  
34 as the location of interlayer species and the layer thickness corresponding to the different  
35 layer types, for all interlayer cations and RH values. From the observed dependence of the  
36 latter parameter on the cation ionic potential ( $\frac{v}{r}$ ,  $v$  = cation valency and  $r$  = ionic radius) and  
37 on RH, the following equations were derived:

38 Layer thickness (1W) =  $12.556 + 0.3525 \times \left( \frac{v}{r} - 0.241 \right) \times (v \times RH - 0.979)$

39 Layer thickness (2W) =  $15.592 + 0.6472 \times \left( \frac{v}{r} - 0.839 \right) \times (v \times RH - 1.412)$

40 which allow the quantification of the increase of layer thickness with increasing RH for both  
41 1W (one-water) and 2W (two-water) layers. In addition for 2W layers interlayer H<sub>2</sub>O  
42 molecules are probably distributed as a unique plane on each side of the central interlayer  
43 cation. This plane of H<sub>2</sub>O molecules is located at ~1.20 Å from the central interlayer cation  
44 along the  $c^*$  axis.

45

45 **INTRODUCTION**

46

47 Bentonite has been long used as buffer material for engineered barriers in municipal  
48 waste disposal sites because of its low permeability when compacted and because of its  
49 cation-retention ability. These properties also make bentonite a possible buffer material in  
50 multi-barrier designs for nuclear waste repositories. Specifically, bentonite may be used to  
51 isolate intermediate-level long-lived wastes (ILLW wastes) from the geological barrier, and  
52 from the biosphere. The retention and mechanical properties of this material are mainly  
53 influenced by its smectite component. The high smectite content provides bentonite with a  
54 self-healing capacity and the ability to sorb cations, the latter being enhanced by the high  
55 surface area of smectite. Sorption would help limit and/or delay possible radionuclide  
56 migration. Both properties result from the specific hydration/expansion ability of this mineral  
57 component.

58 However, interactions between the nuclear waste package and the bentonite barrier  
59 could possibly alter these properties. For example, concrete as a civil engineering material or  
60 as a component of the waste package will produce alkali-rich high pH aqueous solutions (“pH  
61 plume”) during alteration. The effect of such solutions on smectite has been widely studied  
62 (Mohnot et al. 1987; Carroll-Webb and Walther 1988; Carroll and Walther 1990; Chermak  
63 1992, 1993; Eberl et al. 1993; Huang 1993; Bauer and Berger 1998; Bauer et al. 1998; Bauer  
64 and Velde 1999; Cama et al. 2000; Taubald et al. 2000; Huertas et al. 2001; Rassineux et al.  
65 2001; Claret et al. 2002). Smectite in the bentonite can be affected also by a thermal pulse  
66 resulting from the radioactivity of the waste package. By analogy with burial diagenesis in  
67 sediments (Weaver 1960; Hower and Mowatt 1966; Burst 1969; Perry and Hower 1972;  
68 Hower et al. 1976, etc.) smectite is expected to transform with increasing temperature into  
69 non-expandable illite through intermediate mixed-layer structures. Structural changes of

70 smectites during the early stages of this transformation relate to the location and the amount  
71 of layer charge (Sato et al. 1996; Drits et al. 1997a; Beaufort et al. 2001). Because these  
72 changes probably produce subtle changes of the hydration/expansion properties of the  
73 smectite, which persist throughout subsequent stages of the illitization reaction (Drits et al.  
74 1997a), a careful study of these hydration properties using X-ray diffraction (XRD) is  
75 possibly a way to investigate the early steps of the smectite-to-illite transition. However,  
76 because these properties also vary as a function of the nature of the interlayer cation and of  
77 relative humidity, the influence of these two parameters must be assessed first for reference  
78 smectite samples. In addition, the intrinsic heterogeneity of smectite materials (Calarge et al.  
79 2003; Meunier et al. 2004) can lead to the coexistence within the same crystallite of layers  
80 exhibiting different hydration states. This effect can be quantified by comparing XRD  
81 patterns recorded under stable experimental conditions with patterns calculated assuming a  
82 random interstratification of layers exhibiting different hydration states.

83         This paper reports on a detailed characterization of the hydration properties of a low-  
84 charged montmorillonite reference sample (the Clay Mineral Society source clay, SWy-1).  
85 Following purification and size fractionation, aliquots of the <1- $\mu\text{m}$  size fraction of this  
86 reference sample were saturated with  $\text{K}^+$ ,  $\text{Na}^+$ ,  $\text{Li}^+$ ,  $\text{Sr}^{2+}$ ,  $\text{Ca}^{2+}$  and  $\text{Mg}^{2+}$  interlayer cations.  
87 Experimental XRD patterns were recorded at fixed relative humidity (RH) conditions over a  
88 range from an essentially dry atmosphere ( $\sim 0\%$  RH) to approximately 80% RH. Experimental  
89 XRD patterns were compared to calculated models for each cation and each relative humidity  
90 to obtain the proportion of layers with defined hydration states. Additional structural  
91 parameters, such as the thickness of hydrated layers, the distribution of interlayer  $\text{H}_2\text{O}$   
92 molecules were also assessed with this modeling approach.

93

94 **BACKGROUND**

95

96 The ability of some 2:1 phyllosilicates, including smectites, to incorporate interlayer  
97 H<sub>2</sub>O molecules and the subsequent change in basal spacing has been extensively studied for  
98 several decades. For example, Nagelschmidt (1936) and Bradley et al. (1937) showed by  
99 XRD that the basal spacing of smectite increases in steps as the amount of water increases in  
100 the sample environment. These discrete steps were later attributed to the intercalation of 0, 1,  
101 2 or 3 planes of H<sub>2</sub>O molecules in the smectite interlayer (Mooney et al. 1952; Méring and  
102 Glaeser 1954; Norrish 1954; Walker 1956). From these pioneering studies, hydration  
103 properties of 2:1 phyllosilicates (smectites) were shown to be controlled by such factors as the  
104 type of the interlayer cation, and the amount and the location of layer charge (octahedral or  
105 tetrahedral sites). These observations suggested several possible models where crystalline  
106 swelling is controlled by the balance between the repulsive force owing to 2:1 layer  
107 interactions and the attractive forces between hydrated interlayer cations and the negatively  
108 charged surface of siloxane layers (Norrish 1954; Van Olphen 1965; Kittrick 1969a, 1969b;  
109 Laird 1996, 1999).

110 Smectite hydration properties are often characterized by XRD from the evolution of  
111 *d*(001) basal-spacing value under variable RH (Méring and Glaeser 1954; Harward and  
112 Brindley 1965; Glaeser and Méring 1967, 1968; Harward et al. 1969; Watanabe and Sato  
113 1988; Sato et al. 1992; Yamada et al. 1994; Tamura et al. 2000, among others). Modeling  
114 techniques complement this approach. For example, Ben Brahim et al. (1983a, 1983b, 1984)  
115 studied the interlayer structure (atomic positions of interlayer cations and associated H<sub>2</sub>O  
116 molecules) of Na-saturated montmorillonite and beidellite samples.

117 However, these studies systematically assume homogeneous hydration conditions for  
118 a given cation at a given RH whereas the coexistence of different hydration states in a sample

119 is probably common even under controlled conditions (Méring and Glaeser 1954; Glaeser and  
120 Méring 1967; Sato et al. 1992, 1996). For example, the irrational character of the  $d(00\ell)$   
121 reflection series at the transition between two discrete hydration states and the asymmetric  
122 profiles of high-angle reflections indicate such coexistence, most likely arising from a  
123 heterogeneous layer-charge distribution (Sato et al. 1992). Few studies have taken into  
124 account the coexistence of layers with contrasting layer thickness corresponding to different  
125 hydration states. Moore and Hower (1986) studied ordered structures composed of mono-  
126 hydrated and collapsed interlayers in montmorillonite and Cuadros (1997) estimated the H<sub>2</sub>O  
127 content of smectite as a function of the interlayer cation. Using a similar approach, Iwasaki  
128 and Watanabe (1988) were able to investigate the distribution of Na<sup>+</sup> and Ca<sup>2+</sup> cations over  
129 the interlayers of smectite and smectite-illite mixed-layer structures. Assessing the cationic  
130 composition of smectite interlayers from the layer thickness (~15.0 and 12.5 Å for Ca<sup>2+</sup> and  
131 Na<sup>+</sup>, respectively) Iwasaki and Watanabe (1988) demonstrated that Na<sup>+</sup> and Ca<sup>2+</sup> cations  
132 occur in different interlayers leading to the presence of segregated domains. These domains  
133 are reminiscent of the “demixed state” described in the early works of Glaeser and Méring  
134 (1954), Levy and Francis (1975) and Mamy and Gaultier (1979).

135 Bérend et al. (1995) and Cases et al. (1997) applied such a XRD profile modeling  
136 approach in combination with adsorption-desorption isotherm experiments to assess the  
137 proportion of the different layer types (with 0-3 planes of interlayer H<sub>2</sub>O molecules)  
138 coexisting along the isotherms. However, their calculations were limited to reproduce the  
139 position of the 001 reflection, whereas positions and shapes of higher-order 00 $\ell$  reflections  
140 were not considered. These limitations did not allow a complete description of the real  
141 structure of their samples. More recently, Calarge et al. (2003) and Meunier et al. (2004)  
142 refined this approach by fitting both positions and profiles of the 00 $\ell$  reflections over a large

143 angular range and showed that randomly interstratified structures, each containing different  
144 layer types, coexisted in their montmorillonite samples.

145 To our knowledge, no study has described the interlayer structure of smectite as a  
146 function of RH for the different layer types, and possibly for different cations. The interlayer  
147 structure was determined for 0-3 planes of interlayer H<sub>2</sub>O over a limited RH range for which  
148 the hydration of smectite is considered to be homogeneous. However, the coexistence of  
149 different layer types over an extended RH range has not allowed the interlayer structure to be  
150 determined as a function of RH. Furthermore, in most studies of hydration heterogeneity of  
151 smectite, the structure of the interlayer H<sub>2</sub>O has not been refined because the XRD profile  
152 fitting was usually performed over a limited angular range.

153

## 154 MATERIAL AND METHODS

155

### 156 Sample preparation

157 The smectite used for this study is the SWy-1 montmorillonite reference from the  
158 Source Clay Repository of The Clay Mineral Society with structural formula (Stucki et al.  
159 1984): [(Al<sub>2.99</sub> Fe<sub>0.43</sub> Mg<sub>0.52</sub>)(Si<sub>7.97</sub> Al<sub>0.03</sub>)O<sub>20</sub>(OH)<sub>4</sub>] M<sup>+</sup><sub>0.70</sub> (<2- $\mu$ m size fraction) This  
160 montmorillonite is originally Na-saturated, and exhibits a low octahedral charge and  
161 extremely limited tetrahedral substitutions (Mermut and Lagaly 2001).

162 Size fractionation was performed by centrifugation to obtain a suspension of the  
163 <1  $\mu$ m size fraction. Each ion exchange was made at room temperature with 1 mol.L<sup>-1</sup>  
164 aqueous solutions of K-, Na-, Li-, Ca-, and Sr-chlorides, respectively. SWy-1 suspensions in  
165 each saline solution (~50mg of solid in ~50mL of solution) were shaken mechanically for 24h  
166 before separation of the solid fraction by centrifugation and addition of fresh saline solution.  
167 These steps were repeated three times to ensure a complete cation exchange. Removal of the



168 excess chloride was performed by washing the solid three times by immersion for 24h in  
169 distilled water (Milli-Q /  $18.2 \text{ M}\Omega \text{ cm}^{-1}$ ). The Mg-saturated sample was obtained using a  
170  $0.5 \text{ mol}\cdot\text{L}^{-1}$  solution of magnesium perchlorate to ensure the complete dissociation of the  
171  $\text{Mg}(\text{ClO}_4)_2$  complex in water. Ten steps consisting of a 24h contact between the solution and  
172 the solid followed by centrifugation and renewal of the saline solution guaranteed the  
173 complete saturation before the three steps of washing. These samples are hereafter referred to  
174 as K-, Na-, Li-, Sr-, Ca-, and Mg-SWy-1.

175

### 176 **X-ray diffraction**

177 Oriented slides were prepared for each sample by drying at room temperature a  
178 pipetted clay slurry covering a glass slide. XRD patterns were then recorded using a Siemens  
179 (Bruker) D5000 diffractometer using  $\text{Cu K}\alpha$  radiation and equipped with an Ansyco rh-plus  
180 2250 humidity control device coupled to an Anton Paar TTK450 chamber. Usual scanning  
181 parameters were  $0.04^\circ 2\theta$  as step size and 6s as counting time per step over the  $2\text{-}50^\circ 2\theta$   
182 angular range. The divergence slit, the two Soller slits, the antiscatter and resolution slits were  
183  $0.5^\circ$ ,  $2.3^\circ$ ,  $2.3^\circ$ ,  $0.5^\circ$  and  $0.06^\circ$ , respectively. The relative humidity range used in the present  
184 study extends from almost saturated conditions (80% RH) to extremely dry conditions ( $\sim 0\%$   
185 RH), the latter being obtained by evacuating the entire Paar chamber to a secondary vacuum  
186 ( $\sim 10^{-4}$  Pa). For all samples, XRD patterns were first recorded under room conditions (297 K,  
187 and  $\sim 35\%$  RH), which were controlled (RH) or monitored (temperature) and found stable  
188 over the entire data collection period. Then, XRD patterns were recorded for all samples  
189 following the same sequence of RHs (40, 60, 80%, 20% and 0%) to avoid a possible  
190 irreversible collapse of some layers at low RH values. For any given sample, all six  
191 experimental XRD patterns were recorded within a timeframe that did not exceed 48 hours

192 after the drying of the oriented preparation. This procedure avoided any kinetically driven  
193 dehydration process to occur.

194 The algorithms developed initially by Drits and Sakharov (1976) and more recently  
195 by Drits et al. (1997a) and Sakharov et al. (1999) were used to fit experimental XRD profiles  
196 over the  $2-50^{\circ}2\theta$  range using a trial-and-error approach. Instrumental and experimental  
197 factors such as horizontal and vertical beam divergences, goniometer radius, length and  
198 thickness of the oriented slides were measured and introduced without further adjustment.  
199 The mass absorption coefficient ( $\mu^*$ ) was set to 45, as recommended by Moore and Reynolds  
200 (1997, p. 361), whereas the parameter characterizing the preferred orientation of the sample  
201 ( $\sigma^*$ ) was considered as a variable parameter as discussed below. The  $z$  coordinates for all  
202 atomic positions within the 2:1 layer framework were set as proposed by Moore and Reynolds  
203 (1997, p. 368), but  $z$  coordinates of interlayer species were further refined to improve the  
204 quality of fit. Additional variable parameters include the coherent scattering domain size  
205 (CSDS) along the  $c^*$  axis which was characterized by a maximum CSDS, set to 45 layers, and  
206 by a variable mean CSDS value ( $N$ , Drits et al. 1997b). In addition, because of the weak  
207 bonding between adjacent smectite layers, the layer spacing likely deviates from its average  
208  $d(001)$  value. This cumulative deviation from periodicity was described as “disorder of the  
209 second type” by Guinier (1964) and detailed later by Drits and Tchoubar (1990) and (Drits et  
210 al. (2005), and can be considered as crystal strain. A variance parameter  $\sigma_z$  was introduced to  
211 account for this strain. The effect of  $\sigma_z$  on the profiles of calculated XRD patterns is  
212 illustrated in Figure 1 for Ca-SWy-1 exhibiting a homogeneous hydration state with a layer  
213 thickness of 15.10 Å. When  $\sigma_z$  increases from zero (which corresponds to an ideal periodic  
214 structure) to 0.3 Å, the resulting high-angle maxima are significantly broadened. Moreover,  
215 their relative intensity is decreased as compared to low-angle reflections that are basically

216 unaffected (Fig. 1). The overall fit quality was assessed using the unweighted  $R_p$  parameter  
217 (Howard and Preston 1989):

$$218 \quad R_p = \sqrt{\frac{\sum [I_{obs}(2\theta_i) - I_{calc}(2\theta_i)]^2}{\sum I_{obs}(2\theta_i)^2}} \quad \text{Equation 1}$$

219 where  $I_{obs}$  and  $I_{calc}$  represent measured and calculated intensities, respectively, at position  $2\theta_i$ ,  
220 the subscript  $i$  running over all points in the refined angular range. This parameter is mainly  
221 influenced by the most intense diffraction maxima, such as the 001 reflection, which contains  
222 essential information on the proportions of the different layer types and on their layer  
223 thickness.

224

### 225 **Fitting strategy**

226 XRD-pattern modeling was performed assuming the possible presence of different  
227 layer types. These different layer types correspond to the different hydration states commonly  
228 reported in smectites as a function of relative humidity. In the fitting process, we have  
229 introduced dehydrated layers (0W layers, layer thickness at 9.6-10.1 Å), mono-hydrated  
230 layers with one plane of H<sub>2</sub>O molecules in the interlayer (1W layers at 12.3-12.7 Å), and bi-  
231 hydrated layers with two planes of H<sub>2</sub>O molecules in the interlayer (2W layers at 15.1-  
232 15.8 Å). Because we did not consider RH values greater than 80%, no evidence for tri-  
233 hydrated layers (3W layers at 18.0-18.5 Å) was observed. If a good fit was not obtained with  
234 a unique periodic structure corresponding to one of the layer types, it was first assumed that  
235 this contribution is related to a randomly interstratified mixed-layer structure containing  
236 different layer types. If necessary, additional contributions, each containing different layer  
237 types in variable proportions, were introduced to reproduce the experimental XRD pattern.  
238 However, the use of two mixed-layer structures to fit all features of experimental XRD  
239 patterns does not imply the actual presence of two populations of particles in the sample as

240 discussed below. As a consequence, layers in the same hydration state that are present in the  
241 different mixed-layer structures must have identical properties at a given RH value. Each  
242 given layer type was thus assigned a unique chemical composition, a unique layer thickness  
243 value, and a unique set of atomic coordinates for all mixed-layer structures at a given RH.  
244 Similarly, identical values of  $\sigma^*$ ,  $N$  and  $\sigma_z$  parameters were used for all mixed-layer structures  
245 at a given RH. Each parameter was allowed to vary as a function of relative humidity. The  
246 relative proportions of each mixed-layer structure and of each layer type in these structures  
247 were varied to fit experimental XRD patterns. Following Bérend et al. (1995) and Cases et al.  
248 (1997), the strategy used for XRD profile modeling was to match closely the 001 reflection of  
249 SWy-1 using a mixed-layer structure as homogeneous as possible, i.e., containing as few  
250 different layer types as possible. If necessary to obtain a good fit, a second mixed-layer  
251 structure was introduced to better match the calculated and experimental patterns, and to  
252 better account for the hydration heterogeneity of the sample. This strategy is illustrated in  
253 Figure 2 using the XRD pattern obtained for K-SWy-1 at 0% RH (Fig. 2).

254         The pattern exhibits four major diffraction maxima with positions that do not deviate  
255 much from those expected for a rational series. However, significant asymmetry is observed  
256 on the low-angle side of the first maximum and on the high-angle side of the third maximum.  
257 The second maximum exhibits significant tail broadening (arrows on Fig. 2a). The difference  
258 plot between the experimental pattern and that calculated for dehydrated smectite (100% of  
259 0W layers) shows maxima corresponding to the features mentioned above (Fig. 2b). It was  
260 not possible to reproduce these specific features with a single contribution corresponding to a  
261 mixed-layer structure. Rather, comparison between the positions of the maxima present on  
262 this difference plot with those corresponding to 0W (light gray ticks) and to 1W (dark gray  
263 ticks) smectite and the use of Méring's principle (Méring 1949) suggest that they are probably  
264 related to a mixed-layer structure containing these two layer types. This result arises from

265 coincidence between the features of the difference plot and the arrows. This depiction shows  
266 the position and breadth of the diffraction maxima of a mixed-layer structure as expected  
267 from Méring's principle (Fig. 2b). Two structures thus appear to be present: the initial  
268 structure (S1, 100% 0W layers) and a second (S2). The latter results from the random  
269 interstratification of 0W and 1W layers (70% and 30%, respectively). A good fit ( $R_p =$   
270 3.73%) is obtained assuming a 81:19 ratio between S1 and S2 (Fig. 2c). A schematic of this  
271 result is given in Figure 2d where the relative proportions of the two structures contributing to  
272 the diffraction intensity are illustrated along the vertical axis by their respective surface areas  
273 in the square box whereas the proportion of the different layer types in each mixed-layer  
274 structure is represented on the horizontal axis.

275 Note that calculated XRD patterns are not plotted in the low-angle region ( $2\theta$  angles  
276 lower than  $7^\circ$  in the present case) because the computed "background" shape in this region is  
277 not compatible with that measured on experimental patterns. The origin of this discrepancy is  
278 discussed below.

279

280

## RESULTS

281

### 282 Qualitative description of experimental patterns

283 Figure 3 shows the evolution as a function of RH of the  $d(001)$  values measured on  
284 the experimental XRD patterns. These values are also listed in Table 1 together with the full  
285 width at half maximum intensity (FWHM) of the 001 reflection. Table 1 also includes the  
286 standard deviation of the departure from rationality ( $\xi$ ) of the  $00\ell$  reflection series. This latter  
287 parameter is calculated as the standard deviation of the  $\ell \times d(00\ell)$  values calculated for all  
288 measurable reflections over the  $2\theta = 2-50^\circ$  range. On Figure 3, the usual hydration states are  
289 observed for smectites with 0W layers ( $d(001)$  at 9.6-10.1 Å) observed only at 0% RH for

290 Na-, K-, and Sr-SWy-1, 1W layers ( $d(001)$  at 12.3-12.7 Å), 2W layers ( $d(001)$  at 15.0-15.8 Å)  
291 as given by Sato et al. (1992). However, the common coexistence of different hydration states  
292 are identified both from a  $d(00\ell)$  value intermediate between those corresponding to the usual  
293 discrete hydration states (gray domains in Fig. 3) and from a high  $\xi$  value indicating the  
294 irrationality of  $00\ell$  reflections (open symbols in Fig. 3). K-SWy-1, for example, shows mostly  
295 coexisting hydration states in Figure 3. The heterogeneity of hydration states, which leads to  
296 the interstratification of different layer types, produces an increased FWHM of the diffraction  
297 maxima as illustrated in Figure 4 which shows the correlation between the  $\xi$  parameter and  
298 the FWHM measured on the 001 reflection. From Figures 3 and 4, maximum values can be  
299 defined for both the FWHM of the 001 reflection ( $2\theta = 1.1^\circ$ ) and the  $\xi$  parameter (0.4 Å)  
300 limiting the “homogeneous” hydration domains. Values higher than these limits correspond to  
301 an extremely heterogeneous hydration state and/or to the transition between two discrete  
302 hydration states.

303         However, within these “homogeneous” or “heterogeneous” hydration domains  
304 additional structural features can be determined from the careful examination of experimental  
305 XRD patterns (Fig. 5). In particular, within homogeneous 2W domains (Na-SWy-1 and Li-  
306 SWy-1: 80% RH, Sr-SWy-1: 40-80% RH, Ca-SWy-1: 35-80% RH and Mg-SWy-1: 20-80%  
307 RH) the position and the width (FWHM) of the 001 reflection vary as a function of RH  
308 together with the  $\xi$  parameter (Table 1). Specifically, for samples saturated with divalent  
309 cations the  $d(001)$  value increases with increasing RH whereas both the FWHM of the 001  
310 reflection and the  $\xi$  parameter decrease. On experimental XRD patterns, the 002 reflection  
311 appears as a sharp and well-defined reflection only when the values of the latter two  
312 parameters are minimized (Sr-SWy-1: 60-80% RH, Ca-SWy-1: 80% RH and Mg-SWy-1: 60-  
313 80% RH, Figs. 5d, 5e, 5f). The position of the 001 reflection also varies as a function of RH  
314 within homogeneous 1W hydration state (Na-SWy-1: 35-60% RH, Li-SWy-1: 20-60% RH,

315 and Sr-SWy-1: 20-35% RH) whereas other qualitative parameters remain constant for a given  
316 sample (Table 1). A homogeneous dehydrated state is observed only under vacuum conditions  
317 (0% RH) for K-SWy-1, Na-SWy-1 and Sr-SWy-1 samples. The experimental XRD patterns  
318 of these three samples exhibit well-defined sharp 00 $l$  reflections (Figs. 5a, 5b, 5d).

319 In contrast, the presence of important hydration heterogeneities induce specific  
320 features on experimental XRD patterns (K-SWy-1: 20-80% RH, Na-SWy-1: 20% RH, Li-  
321 SWy-1 and Mg-SWy-1: 0% RH, and Ca-SWy-1: 0-20% RH). For example, XRD patterns of  
322 K-SWy-1 over the 20-80% RH range show well-defined reflections only at 11.0-12.0 Å and  
323  $\sim$ 3.25 Å (Fig. 5a). Other reflections appear as broad and diffuse maxima. The sharpness of the  
324  $\sim$ 3.25 Å maximum is related to the proximity between the 003 reflection of dehydrated  
325 smectite ( $\sim$ 3.3 Å) and the 004 reflection of the mono-hydrated smectite ( $\sim$ 3.1 Å). In addition,  
326 note that for higher RH values (40-80% RH) the FWHM of the 001 reflection is at a  
327 maximum although its position is close to the usual position for 1W layers. This result may be  
328 related to the increasing proportion of 2W layers, or to the residual presence of a high  
329 proportion of 0W layers. In the latter case, the shift in position of the 001 reflection induced  
330 by a relatively large proportion of 0W layers is limited because the structure factor of 0W  
331 layers is much smaller than that of 1W layers over the considered angular range, whereas the  
332 interstratification leads to increased FWHM values (Drits et al. 1994). If the heterogeneity is  
333 produced by the presence of 2W layers, the diffraction maximum at  $\sim$ 3.25 Å remains mostly  
334 unaffected as interferences with the 005 reflection of a 2W smectite (at  $\sim$ 3.10 Å) would not  
335 cause broadening. For Na-SWy-1 recorded at 20% RH, the measured irrationality of the 00 $l$   
336 reflection positions is associated, as for K-SWy-1, with a significant broadening of all  
337 diffraction maxima except for the two reflections at  $\sim$ 12.0 Å and  $\sim$ 3.10 Å, which remain sharp  
338 and well defined (Fig. 5b). For Li-SWy-1 at 0% RH, note that even the maximum at  $\sim$ 3.10 Å  
339 is significantly broadened (Fig. 5c). For Ca-SWy-1 at 0% RH, the position of the 001

340 reflection at  $\sim 11.7 \text{ \AA}$  is shifted away from values expected for a 1W smectite. In addition  
341 there is a significant broadening of this reflection ( $2\theta = 1.12^\circ$ , Table 1). Accordingly, the  $\xi$   
342 parameter is relatively large ( $0.50 \text{ \AA}$ , Table 1) and the reflection at  $\sim 2.95 \text{ \AA}$  is poorly defined,  
343 which occurs only when heterogeneous hydration states coexist within the sample. Similar  
344 observations can be made on the XRD pattern recorded for Mg-SWy-1 at 0% RH (Fig. 5f).  
345 For Ca-SWy-1 at 20% RH, the  $\sim 3.1 \text{ \AA}$  peak is even more diffuse, in agreement with the large  
346 values of the FWHM of the 001 reflection and of the  $\xi$  parameter ( $2\theta = 1.24^\circ$  and  $0.93 \text{ \AA}$ ,  
347 respectively, Table 1).

348           Qualitative descriptions such as those above have allowed the determination of the  
349 main hydration states of smectites by using the position of the 001 reflection, and the  
350 characterization of smectite hydration properties as a function of the magnitude and location  
351 of layer charge (Harward and Brindley 1965; Harward et al. 1969; Yamada et al. 1994;  
352 Tamura et al. 2000). Parameters such as FWHM of the 001 reflection, or the irrational  
353 character of  $00l$  reflections provide additional data on the hydration state of these minerals  
354 and especially on their hydration heterogeneity (Watanabe and Sato 1988; Sato et al. 1992).  
355 However, results described above indicate that although the general descriptions are similar  
356 for all parameters, specific features of the XRD patterns, such as the resolution of the 002  
357 reflection for 2W smectite (e.g.), are not accounted for by parametric descriptions.  
358 Furthermore, although these parameters allow the assessment of coexisting smectites layers  
359 with different hydration states in the same sample, they do not provide detailed insight into  
360 this heterogeneity. To achieve this goal, and in particular to determine quantitatively the  
361 relative proportions of the different layer types and their structural characteristics (e.g., layer  
362 thickness and number of interlayer  $\text{H}_2\text{O}$  molecules) the experimental XRD patterns were  
363 modeled using a trial-and-error approach described by Drits and Tchoubar (1990).

364



## 365 **Modeling of X-ray diffraction profiles**

366 XRD patterns were fitted using the strategy described above. Structural models to  
367 obtain optimum fits shown in Figure 5 are described schematically (relative proportion and  
368 composition of the different mixed-layer structure contributions) in Figure 6. The relative  
369 proportions of the different layer types are reported in Figure 7 as a function of RH, whereas  
370 structural parameters are listed in Table 2.

371 **K-SWy-1 sample.** At 0% RH, the optimum model (described in the Methods  
372 section) is consistent with the qualitative description of the sample with a major contribution  
373 from a pure 0W smectite and a minor contribution from a mixed-layer structure containing  
374 0W and 1W layers in a 70:30 ratio (Fig. 6a). The latter mixed-layer structure accounts for the  
375 low-angle asymmetry of the 001 reflection and for the tail broadening of the 002 reflection.  
376 Layer thickness of both 0W and 1W layers (10.0, and 12.4 Å, respectively) are consistent  
377 with published values. The broadening of the second-order diffraction maximum with  
378 increasing RH (Fig. 5a) is related to the increasing proportion of 1W and 2W layers for each  
379 of the two mixed-layer structure contributions (Fig. 6a). The two mixed-layer structures also  
380 account for the increase of the  $\xi$  parameter with increasing RH (Table 1). The increased  
381 proportion of 1W layers with increasing RH produces a shift of the  $\sim 3.25$  Å diffraction  
382 maximum toward higher angles. However, 0W layers are still prevailing at 80% RH, although  
383 the sample was not totally dehydrated before collecting this XRD pattern. At this high RH  
384 value, the position of the 001 reflection (12.04 Å, Table 1) differs significantly from the value  
385 expected for 0W smectite, because of the contrasting structure factors of 0W and 1W layer  
386 types (Drits et al. 1994). The large FWHM value measured for the 001 reflection results likely  
387 from the combination of the large number of 0W layers and of the minor presence of 2W  
388 layers. Structural parameters leading to the optimal fits (Fig. 5a) such as  $\sigma^*$ , N and  $\sigma_z$  do not

389 vary significantly as a function of RH (4-5°, 8-13 layers and 0.20-0.25 Å, respectively, Table  
390 2).

391 **Na-SWy-1 sample.** In agreement with its qualitative description, and with the  
392 presence of sharp and well-defined diffraction maxima, this sample contained a large  
393 proportion of 0W, 1W, and 2W layers at 0%, 35-60, and 80% RH, respectively. At these  
394 different RHs, the main layer type was essentially present in a major mixed-layer structure  
395 exhibiting little, if any, hydration heterogeneity. A minor mixed-layer structure accounts for  
396 most of the hydration heterogeneity. At 0% RH, this minor mixed-layer structure produces  
397 low-angle asymmetry of the 001 reflection and tail broadening of the 002 reflection. From 35-  
398 60% RH, the minor mixed-layer structure accounts for the low-angle asymmetry of the 001  
399 reflection (at ~12.4 Å) and for the broad hump on the high-angle side of the 002 reflection. At  
400 80% RH, the minor mixed-layer structure contributes on the high-angle side of the 001  
401 reflection (~15.3 Å) and also accounts for the slight asymmetries of 003 and 005 reflection  
402 (~5.2 and ~3.1 Å, respectively).

403 As expected from the high values measured for both the FWHM of the 001 reflection  
404 and the  $\xi$  parameter (Table 1), hydration of this sample is more heterogeneous at 20% RH. In  
405 this case, two mixed-layer structures are present in similar proportions, and they both include  
406 at least two layer types in significant proportions. As a result, 1W and 0W layers, which  
407 prevail in this intermediate hydration state, account for 63 and 33% of all layers, respectively  
408 (Figs. 6b, 7b). The two mixed-layer structures contributions describing this experimental  
409 XRD pattern give similar contributions to the diffracted intensity. However, the small  
410 composition difference between the two mixed-layer structures allows for a better fit to the  
411 broadened and diffuse maxima.

412 As a result of experimental constraints, XRD patterns of Na-SWy-1 were collected  
413 from two oriented slides. One was used for the 0% and 20% RH measurements, whereas the

414 other covered the 35-80% RH range. This difference is especially visible on the  $\sigma^*$  value (5-  
415  $6^\circ$ , and  $\sim 3^\circ$  for the 0-20 and 35-80% RH ranges, respectively, Table 2), and possibly on the  $\sigma_z$   
416 parameter. Despite this experimental hiatus, values obtained for all other structural parameters  
417 are consistent throughout the range of RH (Table 2).

418 **Li-SWy-1 sample.** In agreement with the low values of the FWHM of the 001  
419 reflection and of the  $\xi$  parameter (Table 1), XRD patterns recorded for Li-SWy-1 at 20-60%  
420 RH can be satisfactorily reproduced with a main homogeneous 1W smectite and the accessory  
421 contribution of a mixed-layer structure containing all three layer types (Figs. 5c, 6c). The  
422 mixed-layer structure accounts for the slight asymmetry of the 001 reflection and for the  
423 broad hump on the high-angle side of the 002 reflection. The hump increases with increasing  
424 RH from the growing proportion of 2W layers. At 80% RH, 2W layers prevail but each  
425 mixed-layer structure includes a significant proportion of 1W layers, and even a few 0W  
426 layers (Figs. 6c, 7c). The minor mixed-layer structure contribution allows fitting better the  
427 high-angle side of the 001 and 005 peaks, and the low-angle side of the 003 reflection. The  
428 maximum hydration heterogeneity occurs at 0% RH, and a satisfactory fit was achieved by  
429 using two mixed-layer structures contributions (38:62 ratio), each containing 0W and 1W  
430 layers. The main features of these two contributions to the diffracted intensity are similar  
431 although shifted in position as a result of the contrasting proportions of the two layer types  
432 (30, and 50 % of 0W layers respectively). The combination of these similar features and of  
433 their positional shift allowed reproducing the broad and diffuse diffraction maxima obtained  
434 for the second and third order reflections.

435 **Sr-SWy-1 sample.** The sharp and well-defined maxima observed on all XRD  
436 patterns for Sr-SWy-1 were modeled assuming a major homogenous contribution (Figs. 5d,  
437 6d). For example, a homogeneous 2W smectite represents the main contribution over the 60-  
438 80% RH range. In addition to this homogeneous phase, a minor mixed-layer structure,

439 incorporating all three layer types accounts for the broadened tails of all reflections and for  
440 the high-angle side asymmetry of the 001 reflection. At 40% RH, hydration heterogeneity  
441 occurs as expected from the increased  $\xi$  parameter (0.14 Å as compared to 0.06 Å for the 60-  
442 80% RH range, Table 1). For this RH value, 2W layers prevail at ~75% of all smectite layers  
443 (Fig. 7d), but 0W and 1W layers coexist in the two mixed-layer structures contributing to the  
444 calculated pattern. The contributions of these two mixed-layer structures are quite similar,  
445 although their slight positional shift allows reproducing the faint asymmetry and broadening  
446 of the different reflections. From 40 to 80% RH, the intensity of the ~3.1 Å diffraction  
447 maximum decreases whereas the 002 reflection becomes sharper and better defined. The latter  
448 evolution of the peak profiles and intensity is related to the decreasing amount of 1W layers  
449 when 2W layers prevail (Fig. 7d). The decreased intensity of the ~3.1 Å diffraction maximum  
450 results from the increase of layer thickness for 2W layers which induces in turn a decrease of  
451 the structure factor.

452         A RH only 5% lower induces a dramatic hydration change as 1W layers are  
453 prevailing at 35% RH. A pure 1W smectite accounts for about half of the diffracted intensity.  
454 1W layers are also prevailing in the complementary mixed-layer structure. The latter  
455 contribution accounts for the low-angle side asymmetry of the 001 and 004 reflections and for  
456 the high-angle side tail of the 002 reflection. A similar structure model was used to fit the  
457 XRD pattern of Sr-SWy-1 recorded at 20% RH although the mixed-layer structure accounts  
458 for about 60% of the diffracted intensity. The relative contribution of the pure 1W smectite is  
459 decreased. Finally, at 0% RH a unique mixed-layer structure dominated by 0W layers (80% of  
460 the layers) randomly interstratified with 1W layers was considered (Fig. 6d). Note on this  
461 experimental XRD pattern the presence of a broad reflection on the low-angle side of the 001  
462 reflection. This reflection at ~22 Å could possibly correspond to a regular ( $R = 1$  with  
463 maximum possible degree of order) mixed-layer structure containing similar proportions of

464 0W and 1W layers. However, all attempts to include this contribution to the overall fit proved  
465 unsuccessful, most likely because of intrinsic problems in fitting the low-angle region (see the  
466 Discussion section).

467 **Ca-SWy-1 sample.** XRD patterns recorded for the Ca-SWy-1 sample over the 35-  
468 80% RH range were all fitted assuming the coexistence of two mixed-layer structures with  
469 very consistent compositions (Figs. 5e, 6e). The most homogeneous one accounts for ~40% of  
470 the diffracted intensity and contains essentially 2W layers and a few 1W layers whereas the  
471 main mixed-layer structure contains the three layer types. The latter contribution accounts for  
472 the high-angle asymmetry of the 001 reflection, for the broadened tails of the 003 reflection  
473 and for the shift toward lower-angles of the 005 peak. All these features are reduced with  
474 increasing RH as the content of 0W and 1W layers decreases. However, the 002 reflection is  
475 systematically broad as an indication of the significant proportion of 0W and 1W layers in the  
476 structure, in contrast to the Sr-SWy-1 patterns at high RH values.

477 For lower RH values, smectite hydration is more heterogeneous, and the ~3.1 Å  
478 diffraction maximum is diffuse (Fig. 5e). At 0% RH, heterogeneity was described as resulting  
479 from the coexistence of two mixed-layer structures with similar compositions. 1W layers are  
480 prevailing in the two structures despite the essentially dry atmosphere. Differences in the  
481 composition of these two mixed-layer structures were necessary for fitting the broadened tails  
482 of the 00 $l$  reflections. At 20% RH, even though both mixed-layer structures contain the three  
483 layer types their respective contributions to the diffracted intensity are more contrasted, one  
484 being dominated by 1W layers whereas 2W layers prevail in the other one (Fig. 6e). These  
485 two mixed-layer structures equally contribute to the diffracted intensity to fit in particular the  
486 tabular shape of the complex diffraction maximum at ~3.1 Å (Fig. 5e). Both the similar  
487 intensity of these two contributions and their internal heterogeneity induce a significant  
488 irrationality of 00 $l$  reflections (Table 1).

489 **Mg-SWy-1 sample.** Over the 20-80% RH range, one of the two mixed-layer  
490 structures essentially contains 2W layers (90-95%), and its relative amounts increases from  
491 53-81% with increasing RH (Fig. 6f). A peculiar characteristic of the second mixed-layer  
492 structure, in which 2W layers also dominate, is the presence of 0W layers which  
493 systematically prevail over 1W layers. As a result, the 002 reflection is systematically diffuse.  
494 At 60 and 80% RH, the second contribution accounts for the high-angle asymmetry of the 001  
495 reflection, and for the broadened tails of the 003 and 005 reflections. At lower RH (20-40%  
496 RH), experimental XRD patterns are strikingly different from those collected at 60-80% RH  
497 even though the structure models are similar (Fig. 6f). This is mostly due to the dramatic  
498 change in the layer thickness of 2W layers which is decreased to a stable value of 14.2-14.8 Å  
499 over the 20-40% RH range. This leads to a significant shift of the 003 and 005 reflections  
500 toward higher angles and to the strong increase in intensity of the 004 reflection. This increase  
501 results from the variation of the structure factor induced by the layer-thickness modification.  
502 These additional features indicate that the positional shift of the 001 reflection actually results  
503 from a modification of the layer thickness of 2W layers, rather than from the  
504 interstratification of different layer types. This hypothesis is consistent with the values  
505 determined for the FWHM of the 001 reflection and for the  $\xi$  parameter (0.8-1.0° and 0.2-  
506 0.3 Å, respectively, Table 1) which indicate a limited interstratification. For this RH range,  
507 the minor mixed-layer structure contribution accounts for the high-angle asymmetry of 001  
508 and 004 reflections and for the low-angle asymmetry of 003 and 005 ones.

509 At 0% RH, hydration of the Mg-SWy-1 is more heterogeneous with the presence of  
510 two mixed-layer structure contributions, one containing the three layer types and the other  
511 only 0W and 1W layers. The diffraction features of these two mixed-layer structures are quite  
512 similar, and the positional shift resulting from their contrasting compositions allows fitting the  
513 broad and diffuse maxima of the experimental XRD patterns.

514

515

## DISCUSSION

516

### 517 **Hydration properties of SWy-1 as a function of interlayer cation (Ca, Na, K)**

518           The above quantitative description of the smectite hydration evolution is consistent  
519 with previous studies of smectite hydration (Sato et al. 1992, e.g.). The XRD pattern at 0%  
520 RH for sample K-SWy-1 exhibits a rational series of basal reflections because the structure is  
521 dominated by 0W layers (Figs. 3, 7a). A similar dehydrated state was described at 20% RH by  
522 Sato et al. (1992), although in the present study the evolution toward a more hydrated state  
523 occurs at this RH. However, the irrationality limit used by Sato et al. (1992) is not clearly  
524 defined, and the observed differences may result from a different threshold. The marked  
525 hydration heterogeneity observed by these authors over the 20-60% RH range is in agreement  
526 with the present study, but they reported a homogeneous mono-hydrated state at 80% RH in  
527 contrast to the significant proportion of 0W layers reported in the present work.

528           The description of Na-SWy-1 (Sato et al. 1992) is also consistent with the present  
529 data, with the only significant difference being the onset of the hydration process at low RH  
530 values (<20% RH) as observed here. In contrast, Sato et al. (1992) describe the transition  
531 between dehydrated and mono-hydrated states for RH values slightly higher than 20%.  
532 Finally, our study is consistent with that of Sato et al. (1992) for mostly homogeneous bi-  
533 hydrated state for Ca-SWy-1 over the 40-80% RH range, although they described the partial  
534 dehydration to the mono-hydrated state through highly heterogeneous structures for RH  
535 values of < 30%. At 0% RH, the  $d(001)$  value reported by Sato et al. (1992) is similar to our  
536 study, but they report a homogeneous hydration state for this RH in contrast to our results.  
537 Again, this difference may result from a different definition of the irrationality threshold in

538 the two studies. Similar hydration behavior of homoionic SWy-1 has also been reported by  
539 Cases et al. (1992, 1997) and Bérend et al. (1995).

540

#### 541 **Qualitative indicators of smectite hydration heterogeneity**

542 The  $\xi$  parameter, which accounts for the departure from rationality of  $00\ell$  reflections,  
543 is a good indicator of the hydration-state heterogeneity. When heterogeneity increases from  
544 the coexistence of different layer types, this parameter increases significantly in magnitude  
545 (Fig. 8). Figure 8 plots the relative proportion of the prevailing layer type, whatever its nature,  
546 as a function of the  $\xi$  parameter. Note the low proportion of XRD patterns ( $\sim 25\%$ ) that were  
547 modeled with  $>90\%$  of the total layers of one layer type. However, even for homogeneous  
548 samples, there is still a need to account for hydration heterogeneity to obtain a quality fit as  
549 illustrated in Figure 9 for Li- and Mg-SWy-1. In these two samples, the prevailing layer type  
550 (1W, and 2W layers, respectively) account for 92 and 83% of the total layers. However, it is  
551 still necessary to consider other mixed-layer structure.

552 There is an approximately equal proportion of patterns that involve 70% or less of the  
553 total layers attributed to one prevailing layer type as for 90% or more. Thus heterogeneity is  
554 the rule rather than homogeneity for smectite hydration state. From Figure 8, note that the  
555 increasing heterogeneity is correlated with an increase of the  $\xi$  parameter, which is larger than  
556  $0.4 \text{ \AA}$  when the prevailing layer type accounts for  $\sim 70\%$  or less of the total layers. This  
557 parameter is a good indicator of heterogeneity in the hydration state of smectite. The FWHM  
558 of the 001 reflection, which is larger than  $1.1^\circ$  when the  $\xi$  parameter is larger than  $0.4 \text{ \AA}$ , can  
559 also be used for this purpose (Fig. 4). However, the dependence of the FWHM on the CSDS  
560 leads to important variations of the former parameter even for low values of the  $\xi$  parameter.  
561 For example, over a limited 0.00-0.15 range of the  $\xi$  parameter, the FWHM of the 001  
562 reflection scatters from  $0.47\text{-}1.07^\circ 2\theta$  (Table 1). Larger variation of the FWHM parameter can



563 be expected if different samples are used. The use of the irrationality indicator ( $\xi$  parameter)  
564 to characterize hydration heterogeneity is thus preferable as recommended by Bailey (1982).  
565 However, the FWHM of the 001 reflection can be used as an alternative indicator of hydration  
566 heterogeneity by taking into account the evolution of  $00\ell$  reflection FWHM as a function of  
567 the  $\ell$  index. After correction by  $\cos \theta$  to take into account crystal-size broadening, the FWHM  
568 of  $00\ell$  reflections should be about constant if hydration is homogeneous. Conversely, if  
569 hydration heterogeneity is important the evolution of this parameter is irregular.

570 In addition, in specific cases, hydration heterogeneity can be deduced directly from  
571 specific features of the experimental XRD patterns, related to  $00\ell$  line broadening. When  
572 heterogeneity arises from the coexistence of 0W and 1W layers (e.g. K-SWy-1 for RH = 20-  
573 80% and Na-SWy-1 at RH = 20%) there is no well-defined maximum on experimental XRD  
574 patterns between the 001 reflection (10.2-12.0 Å) and the maximum at  $\sim 3.1$ - $3.2$  Å. If  
575 heterogeneity results from the coexistence of 1W and 2W layers (e.g. Ca-SWy-1 at 20% RH),  
576 the maximum at  $\sim 3.1$  Å is most affected and becomes broad. Finally, for highly hydrated  
577 smectite samples, a small proportion of 1W layers may be easily detected from the  
578 broadening of the 002 reflection at  $\sim 7.6$  Å (e.g., see Sr-SWy-1 at 40 and 60% RH in Fig. 5d).

579

## 580 **Smectite structure as a function of the nature of the interlayer cation and of relative** 581 **humidity**

582 **Assessment of the smectite structure model.** For almost all smectite samples  
583 described here, we considered two distinct contributions to the XRD profiles. These two  
584 contributions is a simplified approach to describe the hydration heterogeneity of the sample  
585 under investigation, with different layer types not being distributed at random in the different  
586 crystallites. The excellent quality of the fits clearly suggests that the proposed model is  
587 realistic. However, the use of two mixed-layer structures to fit all features of the XRD

588 patterns does not imply the actual presence of two populations of particles in the sample.  
589 Accordingly, the relative proportions of the different mixed-layer structures contributing to  
590 the diffracted intensity vary as a function of RH (Fig. 6). As a consequence, layers exhibiting  
591 the same hydration state that are present in the different mixed-layer structures have identical  
592 properties (Table 2) as they may be accounted for in one structure or the other depending on  
593 the RH.

594 **Influence of the affinity of the interlayer cation for water.** For a given RH, the  
595 relative proportion of the different layer types as a function of the cation ionic potential  
596 (valency over ionic radius ratio, Fig. 10) may be given. Ionic radii considered here are given  
597 by Shannon (1976) for octahedrally coordinated cations (1.38, 1.02, 0.76, 1.18, 1.00, and  
598 0.72 Å for  $K^+$ ,  $Na^+$ ,  $Li^+$ ,  $Sr^{2+}$ ,  $Ca^{2+}$ , and  $Mg^{2+}$ , respectively). At 0% RH, 0W layers prevail in  
599 K-, Na- and Sr-SWy-1, whereas Li-, Ca-, and Mg-SWy-1 are dominated by 1W layers. In Ca-  
600 and Mg-SWy-1, some 2W layers are present despite the dry atmosphere. When increasing RH  
601 to 20%, only K-SWy-1 remains mostly dehydrated, in agreement with its low affinity for  $H_2O$   
602 among the studied cations, whereas Na-, Li-, and Sr-SWy-1 are dominated by 1W layers.  
603 Even at RH = 20%, Mg-SWy-1 is mostly bi-hydrated, in agreement with its high affinity for  
604  $H_2O$ , whereas Ca-SWy-1 exhibits an intermediate hydration state between 1W and 2W. At  
605 35% RH, the only significant difference is the hydration state of Ca-SWy-1 which is  
606 essentially bi-hydrated, whereas Sr-SWy-1 becomes so at 40% RH.. Finally, at 80% RH, all  
607 samples are primarily bi-hydrated except K-SWy-1, which is dominated by 0W and 1W  
608 layers in agreement with the low affinity of  $K^+$  for  $H_2O$ . From the above results, the cation  
609 ionic potential, which is directly related to the affinity of the cation for  $H_2O$ , allows a direct  
610 comparison of the results obtained for all cations.

611 **Evolution of layer thickness with relative humidity.** Except for the omnipresence  
612 of hydration heterogeneity, the modeling of experimental XRD patterns collected for a given

613 interlayer cation requires the consideration of variable layer-to-layer distance (i.e., layer  
614 thickness) over the 0-80% RH range for a given layer type (1W, and 2W layers, Table 2). The  
615 layer thickness is greater with increasing RH for all samples, whatever the interlayer cation  
616 (Table 2). For samples displaying a stable and homogeneous hydration state over a large RH  
617 interval (e.g., Li- and Mg-SWy-1) such an increase in layer thickness allowed to describe the  
618 XRD patterns with a consistent structure model. In particular, it was possible to reproduce the  
619 steady evolution of peak position without considering major interstratification effects. For 1W  
620 layers, the increase of layer thickness is associated with an increased number of interlayer  
621 H<sub>2</sub>O molecules, except for K-SWy-1 at medium-to-high RH values. This apparent  
622 inconsistency likely arises from the enhanced sensitivity of XRD to the basal spacing of the  
623 different layer types as compared to their structure factors. As a consequence, layer thickness  
624 has been systematically adjusted during the fitting process, whereas the amount of interlayer  
625 H<sub>2</sub>O was modified only when significant misfits were observed. A similar increase of  
626 interlayer H<sub>2</sub>O molecules and layer thickness is observed for 2W layers. However, for  
627 monovalent cations the precision of the structural parameters determined for 2W layers is low  
628 because of their low abundance (except at 80% RH for Na<sup>+</sup> and Li<sup>+</sup>).

629         The interlayer thickness (IT), that is the layer thickness minus the thickness of the  
630 2:1 layer (6.54 Å), is divided by the cation ionic radius and plotted as a function of RH (Fig.  
631 11a). For each cation, a linear correlation was obtained between the weighted IT and the RH  
632 value, which is expressed as:

$$633 \quad \frac{IT}{r} = a \times RH + b \quad \text{Equation 2}$$

634 where RH is expressed in % RH, r is the cation ionic radius expressed in Å, a and b represent  
635 the slope and axial intercept, respectively. The regression lines obtained for the different  
636 cations (Fig. 11a) show that their slopes increase with increasing cation ionic potential as  
637 indicated, for example, by the comparison between Mg-SWy-1 and Na-SWy-1. For both 1W

638 and 2W layers, monovalent and divalent cations were compared by plotting these slopes as a  
 639 function of the ionic potential (Fig. 11b), and successfully fitting a second order polynomial  
 640 function to this data with ( $r^2 \sim 0.99$ ):

$$641 \quad a_{1W} = 3.525 \cdot 10^{-1} \times \frac{v^2}{r^2} - 0.851 \cdot 10^{-1} \times \frac{v}{r} \quad \text{Equation 3}$$

$$642 \quad a_{2W} = 6.472 \cdot 10^{-1} \times \frac{v^2}{r^2} - 5.433 \cdot 10^{-1} \times \frac{v}{r} \quad \text{Equation 4}$$

643 where  $v$  is the cation valency. IT values weighted for the cation ionic radius obtained at 0%  
 644 RH from the linear regression relationships shown in Figure 11a also correlates with the ionic  
 645 potential for both 1W and 2W layer types ( $r^2 = 0.95$  for the two linear regressions, Fig. 11c)  
 646 leading to the following relations:

$$647 \quad b_{1W} = -0.345 \times \frac{v}{r^2} + 6.099 \times \frac{1}{r} \quad \text{Equation 5}$$

$$648 \quad b_{2W} = -0.914 \times \frac{v}{r^2} + 9.819 \times \frac{1}{r} \quad \text{Equation 6}$$

649 From the combination of the above two regression relations, it was thus possible to  
 650 derive equations relating layer thickness to the RH value and to the ionic potential of cations:

$$651 \quad \text{Layer thickness (1W)} = 12.639 - 0.345 \times \frac{v}{r} - 0.851 \cdot 10^{-1} \times v \times \text{RH} + 3.525 \cdot 10^{-1} \times \frac{v^2 \text{RH}}{r} \quad \text{Equation 7}$$

$$652 \quad \text{Layer thickness (2W)} = 16.359 - 0.914 \times \frac{v}{r} - 5.433 \cdot 10^{-1} \times v \times \text{RH} + 6.472 \cdot 10^{-1} \times \frac{v^2 \text{RH}}{r} \quad \text{Equation 8}$$

653 which can be transformed to:

$$654 \quad \text{Layer thickness (1W)} = 12.556 + 0.3525 \times \left( \frac{v}{r} - 0.241 \right) \times (v \times \text{RH} - 0.979) \quad \text{Equation 9}$$

$$655 \quad \text{Layer thickness (2W)} = 15.592 + 0.6472 \times \left( \frac{v}{r} - 0.839 \right) \times (v \times \text{RH} - 1.412) \quad \text{Equation 10}$$

656           These equations allow the quantification of the steady increase of layer thickness  
657 with increasing RH for both 1W and 2W layers. Because the ionic potential of all cations  
658 considered here is higher than 0.241, the 1W layer-thickness value will increase  
659 systematically with increasing RH for all cations. For monovalent cations, 12.556 Å  
660 represents a maximum layer-thickness value for 1W layers whereas larger layer-thickness  
661 values may be obtained for divalent cations over the 50-100% RH range. Similarly, the 2W  
662 layer-thickness value will increase with increasing RH for all cations except K<sup>+</sup>, whose ionic  
663 potential is lower than 0.839 Å. For K-saturated smectite, layer thickness should be about  
664 constant over the whole range of RH.

665           These results are consistent with those reported by Tamura et al. (2000) for synthetic  
666 smectite with a homogeneous layer-charge distribution, as they demonstrated that the  
667 hydration steps characterizing discrete hydration states (0W, 1W, 2W, ... layers) do not  
668 correspond to fixed d-values. However, the present study demonstrates, in contrast to these  
669 authors, that the layer thickness increase also depends on the interlayer cation and on its ionic  
670 potential. From the above equations, it is possible to determine *a priori* the layer thickness for  
671 1W and 2W low-charge montmorillonites for any interlayer cation. The validity of these  
672 equations for smectite with different amounts and location of charge needs to be assessed.  
673 Figures 11 and 12 show that the above regression equations lead to a realistic estimate of the  
674 experimentally determined layer thickness values for all samples except for 1W layers with  
675 interlayer Ca.

676           **Interlayer H<sub>2</sub>O.** As described above, the increase of layer thickness as a function of  
677 RH is associated with an increase of the number of interlayer H<sub>2</sub>O molecules (Table 2).  
678 Although this change was not systematic when comparing from one RH value to another, this  
679 increase was required to describe all XRD patterns. Together with an increase in the  
680 proportion of layers with higher hydration states, the greater number of interlayer H<sub>2</sub>O with

681 increasing RH is essential for the increase in sample hydration. Interlayer H<sub>2</sub>O is best  
682 quantified using water vapor adsorption-desorption isotherms experiments (Cases et al. 1992,  
683 1997; Bérend et al. 1995). With increasing RH, the combination of the average hydration state  
684 of smectite and of the variable amount of interlayer H<sub>2</sub>O molecules determined for each layer  
685 type allows a reasonable estimate of the number of H<sub>2</sub>O molecules in SWy-1 (Fig. 13). The  
686 experimental water vapor adsorption-desorption data are not fitted as closely when a fixed  
687 amount of interlayer H<sub>2</sub>O molecules is considered, as usually assumed in the calculation of  
688 XRD patterns involving hydrated smectites (Moore and Reynolds 1997, Fig. 13).

689         According to Moore and Reynolds (1997), interlayer cations are sandwiched between  
690 partial planes of H<sub>2</sub>O molecules [0.69 H<sub>2</sub>O per O<sub>20</sub>(OH)<sub>4</sub>] located at 0.35 and 1.06 Å from the  
691 cation along the *c*\* axis. A third and denser plane [1.20 H<sub>2</sub>O per O<sub>20</sub>(OH)<sub>4</sub>] is located further  
692 from the central interlayer cation at 1.20 Å along the *c*\* axis. In our study, XRD patterns were  
693 modeled for 2W layers by defining a unique plane of H<sub>2</sub>O molecules on each side of the  
694 central interlayer cation. This plane is located at 1.20 Å from the central interlayer cation  
695 along the *c*\* axis. This plane is analogous to the dense plane of H<sub>2</sub>O molecules of Moore and  
696 Reynolds (1997). By using the hydration heterogeneity determined above for Sr-Swy-1 at  
697 80% RH, it is possible to fit satisfactorily the 001 reflection using the positions of interlayer  
698 species proposed by Moore and Reynolds (1997, Fig. 14). However, the interlayer positions  
699 and the associated interlayer species proposed by Moore and Reynolds (1997) produced an  
700 intensity distribution dramatically different from the experimental data for higher-angle  
701 reflections (Fig. 14). No attempt was made here to further refine the z-coordinate of the H<sub>2</sub>O  
702 plane as a function of interlayer cation ionic radius.

703         **Fluctuation in atomic z-coordinates -  $\sigma_z$  parameter.** Two trends are obtained for  
704 the  $\sigma_z$  parameter (Table 2), which corresponds to fluctuation of layer thickness, obtained for  
705 the different samples. First, high values for  $\sigma_z$  are often observed for highly heterogeneous

706 samples (e.g., Li-SWy-1 at 0% RH, Ca-SWy-1 at 0 and 20% RH). These high values may  
707 result from the incomplete transition of a given interlayer from one hydration state to the next.  
708 As a result different hydration states would coexist within a given interlayer leading to a large  
709 variation of the interlayer thickness.

710         Second, the  $\sigma_z$  parameter is usually significantly higher (0.25-0.52 Å) when the  
711 sample is saturated with divalent cations rather than monovalent cations (0.15-0.25 Å, except  
712 for the Li-SWy-1 sample at 0% RH). This behavior may be related to two possible structural  
713 features. The first feature relates to the valencies of the cations. The density of divalent  
714 cations is half that of monovalent cations, which produces an extremely heterogeneous  
715 distribution of electrostatic interactions between the 2:1 layer and interlayer cations. This  
716 heterogeneous distribution could perhaps induce fluctuations of the layer thickness within a  
717 given interlayer allowed by the flexibility of the 2:1 layers. The second structural feature for  
718 such an increased  $\sigma_z$  parameter probably relates to the affinity of divalent cations for the bi-  
719 hydrated state. The higher layer thickness observed for 2W layers implies weaker electrostatic  
720 interactions between the negatively charged layer and the interlayer cations. Consequently,  
721 the position of interlayer cations with respect to the 2:1 layer is weakly constrained and the  
722 resulting variation of layer thickness from one interlayer to an adjacent interlayer is greater.  
723 However, the affinity of divalent cations for 2W layers is probably a second-order influence  
724 as shown by the low values for the  $\sigma_z$  parameter on Na- and Li-SWy-1 at 80% RH, even  
725 though these two samples are dominated by 2W layers.

726         **Size of the CSD (N) and sample orientation ( $\sigma^*$ ).** The CSD size along the  $c^*$  axis  
727 determined for each sample is globally stable over the entire RH range investigated (Table 2).  
728 However, a small decrease of the CSD size is systematically observed at RH = 0% for  
729 monovalent interlayer cations. Except for the Li-SWy-1 sample, these samples are strongly  
730 dehydrated with a high proportion (>95%) of 0W layers. Such dehydration probably increases

731 porosity, including intra-crystalline porosity, that could reduce the CSD size. This observation  
732 is supported by the non-variance of the N value at low RH for smectite having divalent  
733 interlayer cations (Table 2). Consistently,  $\sigma^*$  values determined for these dehydrated samples  
734 were systematically higher than those adjusted for higher RH values, possibly as a result of  
735 the textural modifications resulting from increased porosity. However, the increase of  $\sigma^*$  is  
736 observed even for SWy-1 samples exchanged with divalent cations, possibly as an early  
737 indication of the ongoing dehydration process.

738 Lower values of N were also determined for each sample at high RH values (60-  
739 80%) possibly as the result of the splitting of some layer stacks induced by the “osmotic”  
740 swelling of some smectite interlayers. No significant change of the sample orientation is  
741 observed at these high RH values pleading for a different origin for the N decrease, as  
742 compared to the low RH conditions. In our study, lower N values may thus possibly indicate  
743 the presence of a small number of 3W layers that are not accounted for in the calculation, but  
744 such layers would disrupt the stacking order. This hypothesis is consistent with the transition  
745 from 2W to 3W smectite which occurs for RH values higher than 90% for Ca-exchanged  
746 smectites (Watanabe and Sato 1988).

747 **Possible improvements to the proposed description.** The fluctuations of N and  $\sigma^*$   
748 described above may also result from the difficulty in fitting the low-angle region of  
749 experimental XRD patterns. The calculated patterns are always intense over this angular range  
750 as compared to experimental ones. The alternative model proposed by Plançon (2002) for the  
751 description of layer stacking in crystals could possibly better account for such textural defects  
752 in the stacking sequences. In this model, particles rather than crystals are considered. Particles  
753 have sizes larger than crystals and contain defects such as cracks, inner-porosity, bent layers,  
754 edge dislocations, etc. These defects disrupt the periodic layer stacking by inducing variations  
755 in the *d*-value that are accounted for in the proposed formalism. XRD patterns calculated



756 using this formalism nearly coincide with those calculated in our study except in the low-  
757 angle region ( $<5^{\circ}2\theta$  Cu  $K\alpha$ , Plançon 2002), and thus do not challenge the structure models  
758 described in the present work. Over the low-angle region, XRD patterns calculated using the  
759 formalism of Plançon (2002) exhibit a much lower background intensity which would fit  
760 better the experimental XRD data. According to this alternative model, the observed decrease  
761 of N is described as the increased frequency of defects whereas the overall size of the  
762 “particles” would probably be constant.

763 In addition, our study shows that the positions and concentrations of interlayer  
764 species proposed by Moore and Reynolds (1997) are incorrect. Although the quality of the  
765 models obtained in our study is satisfactory, structural parameters may possibly be further  
766 refined by utilizing hydration heterogeneity.

767

768

#### ACKNOWLEDGMENTS

769

770 The results presented are a part of a Ph.D. thesis granted by Andra (French National  
771 Agency for Nuclear Waste Disposal). Andra is thanked for the permission to publish this  
772 manuscript and for financial support. BL acknowledges financial support from the  
773 CNRS/PICS709 program, and from the CNRS/SdU “postes rouges” fellowships granted to  
774 BAS. VAD and BAS are grateful to the Russian Science Foundation for partial financial  
775 support. Laurent Michot (LEM, Nancy – France) is thanked for the fruitful discussions about  
776 smectite hydration. The manuscript was much improved by the constructive reviews of Javier  
777 Cuadros, Dougal Mc Carty, and AE Steve Guggenheim, and by the remarks of Emmanuel  
778 Jacquot on an early version of the manuscript. The editorial assistance of AE Steve  
779 Guggenheim is acknowledged.

780

781  
782  
783  
784  
785  
786  
787  
788  
789  
790  
791  
792  
793  
794  
795  
796  
797  
798  
799  
800  
801  
802  
803  
804

**REFERENCES CITED**

Bailey, S.W. (1982) Nomenclature for regular interstratifications. *American Mineralogist*, 67, 394-398.

Bauer, A. and Berger, G. (1998) Kaolinite and smectite dissolution rate in high molar KOH solutions at 35°C and 80°C. *Applied Geochemistry*, 13, 905-916.

Bauer, A. and Velde, B. (1999) Smectite transformation in high molar KOH solutions. *Clay Minerals*, 34, 259-273.

Bauer, A., Velde, B., and Berger, G. (1998) Kaolinite transformation in high molar KOH solutions. *Applied Geochemistry*, 13, 619-629.

Beaufort, D., Berger, G., Lacharpagne, J.C., and Meunier, A. (2001) An experimental alteration of montmorillonite to a di + trioctahedral smectite assemblage at 100 and 200°C. *Clay Minerals*, 36, 211-225.

Ben Brahim, J., Armagan, N., Besson, G., and Tchoubar, C. (1983a) X-ray diffraction studies on the arrangement of water molecules in a smectite. I. Two-water-layer Na-beidellite. *Journal of Applied Crystallography*, 16, 264-269.

Ben Brahim, J., Besson, G., and Tchoubar, C. (1983b) Layer succession and water molecules arrangement in a homogeneous two-water layer Na-smectite. 5th Meeting of the European Clay Groups, p. 65-75, Prague.

----- (1984) Etude des profils des bandes de diffraction X d'une beidellite-Na hydratée à deux couches d'eau. Détermination du mode d'empilement des feuillets et des sites occupés par l'eau. *Journal of Applied Crystallography*, 17, 179-188.

Bérend, I., Cases, J.M., François, M., Uriot, J.P., Michot, L.J., Masion, A., and Thomas, F. (1995) Mechanism of adsorption and desorption of water vapour by homoionic

805 montmorillonites: 2. The  $\text{Li}^+$ ,  $\text{Na}^+$ ,  $\text{K}^+$ ,  $\text{Rb}^+$  and  $\text{Cs}^+$  exchanged forms. *Clays & Clay*  
806 *Minerals*, 43, 324-336.

807 Bradley, W.F., Grim, R.E., and Clark, G.F. (1937) A study of the behavior of montmorillonite  
808 on wetting. *Zeitschrift Kristallographie*, 97, 260-270.

809 Burst, J.F. (1969) Diagenesis of Gulf Coast clayey sediments and its possible relation to  
810 petroleum migration. *American Association of Petroleum Geologists Bulletin*, 53, 73-  
811 93.

812 Calarge, L., Lanson, B., Meunier, A., and Formoso, M.L. (2003) The smectitic minerals in a  
813 bentonite deposit from Melo (Uruguay). *Clay Minerals*, 38, 25-34.

814 Cama, J., Ganor, J., Ayora, C., and Lasaga, C.A. (2000) Smectite dissolution kinetics at 80  
815 degrees C and pH 8.8. *Geochimica & Cosmochimica Acta*, 64, 2701-2717.

816 Carroll, S.A. and Walther, J.V. (1990) Kaolinite dissolution at 25°, 60° and 80°C. *American*  
817 *Journal of Science*, 290, 797-810.

818 Carroll-Webb, S.A. and Walther, J.V. (1988) A surface complex reaction model for the pH-  
819 dependence of corundum and kaolinite dissolution. *Geochimica & Cosmochimica Acta*,  
820 2609-2623.

821 Cases, J.M., Bérend, I., Besson, G., François, M., Uriot, J.P., Thomas, F., and Poirier, J.P.  
822 (1992) Mechanism of adsorption-desorption of water vapor by homoionic  
823 montmorillonite. 1. The sodium exchanged form. *Langmuir*, 8, 2730-2739.

824 Cases, J.M., Bérend, I., François, M., Uriot, J.P., Michot, L.J., and Thomas, F. (1997)  
825 Mechanism of adsorption and desorption of water vapour by homoionic  
826 montmorillonite: 3. The  $\text{Mg}^{2+}$ ,  $\text{Ca}^{2+}$ ,  $\text{Sr}^{2+}$  and  $\text{Ba}^{2+}$  exchanged forms. *Clays & Clay*  
827 *Minerals*, 45, 8-22.

828 Chermak, J.A. (1992) Low temperature experimental investigation of the effect of high pH  
829 NaOH solutions on the opalinus shale, Switzerland. *Clays & Clay Minerals*, 40, 650-  
830 658.

831 ----- (1993) Low temperature experimental investigation of the effect of high pH KOH  
832 solutions on the Opalinus shale, Switzerland. *Clays & Clay Minerals*, 41, 365-372.

833 Claret, F., Bauer, A., Schafer, T., Griffault, L., and Lanson, B. (2002) Experimental  
834 Investigation of the interaction of clays with high-pH solutions: a case study from the  
835 Callovo-Oxfordian formation, Meuse-Haute Marne underground laboratory (France).  
836 *Clays & Clay Minerals*, 50, 633-646.

837 Cuadros, J. (1997) Interlayer cation effects on the hydration state of smectite. *American*  
838 *Journal of Science*, 297, 829-841.

839 Drits, V.A., Lindgreen, H., Sakharov, B.A., and Salyn, A.S. (1997a) Sequential structure  
840 transformation of illite-smectite-vermiculite during diagenesis of Upper Jurassic shales,  
841 North Sea. *Clay Minerals*, 33, 351-371.

842 Drits, V.A. and Sakharov, B.A. (1976) X-Ray structure analysis of mixed-layer minerals. 256  
843 p. *Dokl. Akad. Nauk SSSR*, Moscow.

844 Drits, V.A., Sakharov, B.A., Salyn, A.L., and Lindgreen, H. (2005) Determination of the  
845 content and distribution of fixed ammonium in illite-smectite using a modified X-ray  
846 diffraction technique: Application to oil source rocks of western Greenland. *American*  
847 *Mineralogist*, 90, in press.

848 Drits, V.A., Srodon, J., and Eberl, D.D. (1997b) XRD measurement of mean crystallite  
849 thickness of illite and illite/smectite: reappraisal of the kubler index and the scherrer  
850 equation. *Clays & Clay Minerals*, 45, 461-475.

851 Drits, V.A. and Tchoubar, C. (1990) X-ray diffraction by disordered lamellar structures:  
852 Theory and applications to microdivided silicates and carbons. 371 p. Springer-Verlag,  
853 Berlin.

854 Drits, V.A., Varaxina, T.V., Sakharov, B.A., and Plançon, A. (1994) A simple technique for  
855 identification of one-dimensional powder X-Ray diffraction patterns for mixed-layer  
856 illite-smectites and other interstratified minerals. *Clays & Clay Minerals*, 42, 382-390.

857 Eberl, D.D., Velde, B., and Mc Cormick, T. (1993) Synthesis of illite-smectite from smectite  
858 at Earth surface temperatures and high pH. *Clay Minerals*, 28, 49-60.

859 Glaeser, P.R. and Méring, J. (1954) Isothermes d'hydratation des montmorillonites bi-  
860 ioniques (Ca, Na). *Clay Mineral Bulletin*, 2, 188-193.

861 Glaeser, R., Mantine, I. and Méring, J. (1967) Observations sur la beidellite. *Bulletin du*  
862 *Groupe Français des Argiles*, 19, 125-130.

863 Glaeser, R. and Méring, J. (1968) Domaines d'hydratation des smectites. *Comptes-Rendus de*  
864 *l'Académie des Sciences de Paris*, 267, 463-466.

865 Guinier, A. (1964) *Théorie et technique de la radiocristallographie*. 740 p. Dunod, Paris.

866 Harward, M.E. and Brindley, G.W. (1965) Swelling properties of synthetic smectites in  
867 relation to lattice substitutions. *Clays & Clay Minerals*, 13, 209-222.

868 Harward, M.E., Carstea, D.D., and Sayegh, A.H. (1969) Properties of vermiculites and  
869 smectites: expansion and collapse. *Clays & Clay Minerals*, 16, 437-447.

870 Howard, S.A. and Preston, K.D. (1989) Profile fitting of powder diffraction patterns. In D.L.  
871 Bish, and J.E. Post, Eds. *Modern Powder Diffraction*, 20, p. 217-275. Mineralogical  
872 Society of America, Washington D.C.

873 Hower, J., Eslinger, E.V., Hower, M.E., and Perry, E.A. (1976) Mechanism of burial  
874 metamorphism of argillaceous sediments: 1. Mineralogical and chemical evidence.  
875 *Geological Society of America Bulletin*, 87, 725-737.

876 Hower, J. and Mowatt, T.C. (1966) The mineralogy of illites and mixed-layer  
877 illite/montmorillonites. *American Mineralogist*, 51, 825-854.

878 Huang, W.L. (1993) The formation of illitic clays from kaolinite in KOH solution from 225°C  
879 to 350°C. *Clays & Clay Minerals*, 41, 645-654.

880 Huertas, F.J., Caballero, E., de Cisneros, C.J., Huertas, F., and Linares, J. (2001) Kinetics of  
881 montmorillonite dissolution in granitic solutions. *Applied Geochemistry*, 16, 397-407.

882 Iwasaki, T. and Watanabe, T. (1988) Distribution of Ca and Na ions in dioctahedral smectites  
883 and interstratified dioctahedral mica/smectites. *Clays & Clay Minerals*, 36, 73-82.

884 Kittrick, J.A. (1969a) Interlayer forces in montmorillonite and vermiculite. *Soil Science  
885 Society of America Journal*, 33, 217-222.

886 ----- (1969b) Quantitative evaluation of the strong-force model for expansion and  
887 contraction of vermiculite. *Soil Science Society of America Journal*, 33, 222-225.

888 Laird, D.A. (1996) Model for crystalline swelling of 2:1 phyllosilicates. *Clays & Clay  
889 Minerals*, 44, 553-559.

890 ----- (1999) Layer charge influences on the hydration of expandable 2:1 phyllosilicates.  
891 *Clays & Clay Minerals*, 47, 630-636.

892 Levy, R. and Francis, C.W. (1975) Demixing of sodium and calcium ions in montmorillonite  
893 crystallites. *Clays & Clay Minerals*, 23, 475-476.

894 Mamy, J. and Gaultier, J.P. (1979) Etude comparée de l'évolution des montmorillonites  
895 biioniques K-Ca de Camp-Berteaux et du Wyoming sous l'effet des cycles  
896 d'humectation et de dessiccation. *Clay Minerals*, 14, 181-192.

897 Méring, J. (1949) L'interférence des rayons-X dans les systèmes à stratification désordonnée.  
898 *Acta Crystallographica*, 2, 371-377.

899 Méring, J. and Glaeser, P.R. (1954) Sur le rôle de la valence des cations échangeables dans la  
900 montmorillonite. Bulletin de la Société Française de Minéralogie et Cristallographie, 77,  
901 519-530.

902 Mermut, A.R. and Lagaly, G. (2001) Baseline studies of The Clay Mineral Society Source  
903 Clays: layer-charge determination and characteristics of those minerals containing 2:1  
904 layers. Clays & Clay Minerals, 49, 393-397.

905 Meunier, A., Lanson, B., and Velde, B. (2004) Composition variation of illite-vermiculite-  
906 smectite mixed-layer minerals in a bentonite bed from Charente (France). Clay  
907 Minerals, 39, 317-332.

908 Mohnot, S.M., Bae, J.H., and Foley, W.L. (1987) A study of alkali/mineral reactions. SPE  
909 Reservoir Engineering, Nov. 1987, 653-663.

910 Mooney, R.W., Keenan, A.G., and Wood, L.A. (1952) Adsorption of water by  
911 montmorillonite. II. Effect of exchangeable ions and lattice swelling as measured by X-  
912 ray diffraction. Journal of American Chemical Society, 74, 1371-1374.

913 Moore, D.M. and Hower, J. (1986) Ordered interstratification of dehydrated and hydrated Na-  
914 smectite. Clays & Clay Minerals, 34, 379-384.

915 Moore, D.M. and Reynolds, R.C., Jr (1997) X-ray Diffraction and the Identification and  
916 Analysis of Clay Minerals. 322 p. Oxford University Press, Oxford and New York.

917 Nagelschmidt, G. (1936) The structure of montmorillonite. Zeitschrift Kristallographie, 93,  
918 481-487.

919 Norrish, K. (1954) The swelling of montmorillonite. Discussions of the Faraday society, 18,  
920 120-133.

921 Perry, E.A., Jr and Hower, J. (1972) Late-stage dehydration in deeply buried pelitic  
922 sediments. American Association of Petroleum Geologists Bulletin, 56, 2013-2021.

923 Plançon, A. (2002) New modeling of X-ray diffraction by disordered lamellar structures, such  
924 as phyllosilicates. *American Mineralogist*, 87, 1672-1677.

925 Rassinoux, F., Griffault, L., Meunier, A., Berger, G., Petit, S., Viellard, P., Zellagui, R., and  
926 Munoz, M. (2001) Expandability-layer stacking relationship during experimental  
927 alteration of a Wyoming bentonite in pH 13.5 solutions at 35 and 60°C. *Clay Minerals*,  
928 36, 197-210.

929 Sakharov, B.A., Lindgreen, H., Salyn, A., and Drits, V.A. (1999) Determination of illite-  
930 smectite structures using multispecimen X-Ray diffraction profile fitting. *Clays & Clay*  
931 *Minerals*, 47, 555-566.

932 Sato, T., Murakami, T., and Watanabe, T. (1996) Change in layer charge of smectites and  
933 smectite layers in illite/smectite during diagenetic alteration. *Clays & Clay Minerals*, 44,  
934 460-469.

935 Sato, T., Watanabe, T., and Otsuka, R. (1992) Effects of layer charge, charge location, and  
936 energy change on expansion properties of dioctahedral smectites. *Clays & Clay*  
937 *Minerals*, 40, 103-113.

938 Shannon, R.D. (1976) Revised effective ionic radii and systematic studies of interatomic  
939 distances in halides and chalcogenides. *Acta Crystallographica*, A 32, 751-767.

940 Stucki, J.W., Golden, D.C., and Roth, C.B. (1984) Effects of reduction and reoxidation of  
941 structural iron on the surface charge dissolution of dioctahedral smectites. *Clays & Clay*  
942 *Minerals*, 32, 350-356.

943 Tamura, K., Yamada, H., and Nakazawa, H. (2000) Stepwise hydration of high-quality  
944 synthetic smectite with various cations. *Clays & Clay Minerals*, 48, 400-404.

945 Taubald, H., Bauer, A., Schafer, T., Geckeis, H., Satir, M., and Kim, J.I. (2000) Experimental  
946 investigation of the effect of high-pH solutions on the Opalinus Shale and the  
947 Hammerschmiede Smectite. *Clay Minerals*, 35, 515-524.



- 948 Van Olphen, H. (1965) Thermodynamics of interlayer adsorption of water in clays. Journal of  
949 Colloid Science, 20, 822-837.
- 950 Walker, G.F. (1956) The mechanism of dehydration of Mg-vermiculite. Clays & Clay  
951 Minerals, 4, 101-115.
- 952 Watanabe, T. and Sato, T. (1988) Expansion characteristics of montmorillonite and saponite  
953 under various relative humidity conditions. Clay Science, 7, 129-138.
- 954 Weaver, C.E. (1960) Possible uses of clay minerals in search for oil. American Association of  
955 Petroleum Geologists Bulletin, 44, 1505-1518.
- 956 Yamada, H., Nakazawa, H., Hashizume, H., Shimomura, S., and Watanabe, T. (1994)  
957 Hydration behavior of Na-smectite crystals synthesised at high pressure and high  
958 temperature. Clays & Clay Minerals, 42, 77-80.
- 959

## FIGURE CAPTIONS

959  
960  
961  
962  
963  
964  
965  
966  
967  
968  
969  
970  
971  
972  
973  
974  
975  
976  
977  
978  
979  
980  
981  
982  
983

**FIGURE 1.** Influence on calculated XRD patterns of the cumulative deviation of the layer thickness from the strict  $d(001)$  periodicity. This deviation is quantified here study with the  $\sigma_z$  parameter. The effect is shown for a XRD pattern calculated for a pure bi-hydrated Ca-SWy-1 sample. Solid line:  $\sigma_z = 0.0 \text{ \AA}$ , gray line:  $\sigma_z = 0.3 \text{ \AA}$ .

**FIGURE 2.** Basic principle of the strategy used to fit experimental XRD patterns (see text for details). **a)** The experimental pattern of sample K-SWy-1 recorded at 0% RH is shown as crosses, whereas the XRD pattern calculated for a pure dehydrated smectite (100% 0W layers) is shown as a gray line. Values in parentheses correspond to  $\ell \times d(00\ell)$  ideal positions. **b)** The maxima of the difference plot between experimental and calculated patterns are located between elementary contributions corresponding to 0W and 1W layer types (light and dark gray ticks, respectively). **c)** The optimum fit to the experimental data, shown as a solid line, consists of a mixture of the initial pure dehydrated structure with a mixed-layer structure (70:30 ratio between 1W and 0W layers). These two elementary contributions are shown as bold gray and solid lines, respectively. **d)** Schematic representation of the structure model used to fit the experimental XRD pattern. Relative proportions, expressed in wt%, of the two elementary mixed-layer structure contributions are plotted on the y-axis whereas their compositions (relative proportions of the different layer types) are plotted on the x-axis. Light gray and dark gray bars represent 0W and 1W layers, respectively.

**FIGURE 3.** Variations of the basal spacing  $d(001)$  measured on experimental XRD patterns as a function of relative humidity for samples saturated with monovalent and divalent cations.  $d(001)$  values are plotted as open symbols when the departure from rationality parameter ( $\xi$ ) determined for the basal reflection series (see text for

984 details) is higher than 0.4 Å. Light gray areas represent commonly reported  $d(001)$   
985 values reported for bi-hydrated ( $d(001)$  at 15.0-15.8 Å), mono-hydrated ( $d(001)$  at  
986 12.3-12.7 Å) and dehydrated smectites ( $d(001)$  at 9.6-10.1 Å).

987 **FIGURE 4.** FWHM of the (001) reflection as a function of the departure from rationality  
988 parameter  $\xi$  (see text for details). Values of these two parameters ( $1.1^\circ 2\theta$  Cu  $K\alpha$ , and  
989 0.4 Å, respectively) limiting the “homogeneous” hydration domains are shown as  
990 dotted lines. Open and solid symbols as in Figure 3.

991 **FIGURE 5.** Comparison between experimental and calculated XRD patterns as a function of  
992 RH. Experimental and calculated optimal XRD patterns are shown as crosses and as  
993 solid lines, respectively. Difference plots are shown at the bottom of the figure. **a)**  
994 Sample K-SWy-1. **b)** Sample Na-SWy-1. **c)** Sample Li-SWy-1. **d)** Sample Sr-SWy-  
995 1. **e)** Sample Ca-SWy-1. **f)** Sample Mg-SWy-1. For Na-, Li-, Sr-, Ca- and Mg-SWy-  
996 1 samples, the gray bar indicates a modified scale factor for the high-angle region.  
997 Dashed lines in Figure 5f indicate the ideal peak positions for 2W smectite (15.8 Å).

998 **FIGURE 6:** Structure models obtained from XRD profiles modeling for all samples as a  
999 function of RH. Symbols and notations as in Figure 2d (solid bars represent 2W  
1000 layers).

1001 **FIGURE 7.** Evolution of the relative abundance of different layer types (including all mixed-  
1002 layer structures) as a function of RH for all samples. **a)** Sample K-SWy-1. **b)** Sample  
1003 Na-SWy-1. **c)** Sample Li-SWy-1. **d)** Sample Sr-SWy-1. **e)** Sample Ca-SWy-1. **f)**  
1004 Sample Mg-SWy-1. Triangles, diamonds, and squares represent 0W, 1W and 2W  
1005 layers, respectively.

1006 **FIGURE 8.** Relative proportion of the major layer type (whatever its nature) derived from  
1007 XRD profile modeling as a function of the departure from rationality parameter  $\xi$ .  
1008 Dotted lines as in Figure 4; solid and open symbols as in Figure 3.

1009 **FIGURE 9.** Comparison between the experimental XRD patterns obtained for Li- and Mg-  
1010 SWy-1 samples at 40% RH and that calculated considering only the most  
1011 homogeneous phase from the optimum structure models reported in Figure 6.

1012 **FIGURE 10.** Relative proportion of the different layer types determined at each RH for the  
1013 different samples. Samples are ranked as a function of their ionic potential ( $v/r$ ).  
1014 Light gray, dark gray and solid bars represent 0W, 1W, and 2W layers, respectively.

1015 **FIGURE 11.** Evolution of layer thickness as a function of RH for all samples. Evolutions for  
1016 1W and 2W layer types are shown on the left and right columns, respectively. **a)**  
1017 Evolution of the interlayer thickness (IT), that is layer thickness minus the thickness  
1018 of the 2:1 layer ( $6.54\text{\AA}$ ), weighted for the cation ionic radius as a function of RH for  
1019 all samples. Linear regression lines are plotted for each cation. **b)** Evolution of the  
1020 slope of the linear regressions shown on Figure 11a as a function of the ionic  
1021 potential of the interlayer cation. A 2<sup>nd</sup> order polynomial regression is fitted to this  
1022 data. **c)** Evolution of the IT weighted for the cation ionic radius at 0% RH obtained  
1023 from the linear regression shown on Figure 11a as a function of the ionic potential of  
1024 the interlayer cation. A linear regression is fitted to this data.

1025 **FIGURE 12.** Comparison between the layer-thickness values determined for 1W and 2W  
1026 layers from Equations 7 and 8, respectively, with that obtained from XRD profile  
1027 modeling. Linear regressions are fitted to the data. **a)** 1W layers. **b)** 2W layers.

1028 **FIGURE 13.** Comparison between the amount of water determined from water vapor  
1029 adsorption-desorption isotherms by Bérend et al. (1995) and Cases et al. (1997) and  
1030 that derived from XRD profile modeling. Adsorption and desorption pathways are  
1031 shown as solid and dashed lines, respectively. Solid and open patterns indicate  
1032 results derived from the modeling of XRD patterns recorded in adsorption and  
1033 desorption conditions, respectively. Triangles indicate results derived from the

1034 modeling of XRD patterns assuming the fixed amount of interlayer H<sub>2</sub>O molecules  
1035 commonly used in the calculation of XRD patterns involving hydrated smectites  
1036 (Moore and Reynolds 1997). Squares indicate results derived from the modeling of  
1037 XRD patterns assuming a variable amount of interlayer H<sub>2</sub>O molecules as described  
1038 here. Gray patterns indicate the starting conditions (~35% RH).

1039

1040 **FIGURE 14.** Comparison of the experimental XRD pattern recorded for Sr-SWy-1 sample at  
1041 80% RH with that calculated using a structure model similar to the optimal one  
1042 (Table 2) but replacing the refined atomic positions for interlayer H<sub>2</sub>O molecules by  
1043 that proposed by Moore and Reynolds (1997). Patterns as in Figure 2a.

TABLES

**TABLE 1.** Evolution of the basal reflection qualitative descriptors (position, width and rationality) as a function of relative humidity.

Sample	K			Na			Li		
	$d(001)$	FWHM	$\xi, X_i$	$d(001)$	FWHM	$\xi, X_i$	$d(001)$	FWHM	$\xi, X_i$
~0%	10.24	1.07	0.14, 3	9.75	0.85	0.07, 4	11.66	1.39	0.52, 3
20%	10.95	1.53	0.64, 3	11.96	1.17	0.53, 4	12.31	0.59	0.04, 4
~35%	11.36	1.57	0.86, 3	12.44	0.68	0.10, 3	12.32	0.58	0.04, 4
40%	11.54	1.51	1.34, 2	12.45	0.66	0.02, 3	12.33	0.59	0.03, 4
60%	11.57	1.51	1.34, 2	12.47	0.72	0.01, 3	12.36	0.66	0.04, 4
80%	12.04	1.82	1.69, 2	15.28	0.75	0.28, 3	15.49	0.73	0.28, 4

Sample	Sr			Ca			Mg		
	$d(001)$	FWHM	$\xi, X_i$	$d(001)$	FWHM	$\xi, X_i$	$d(001)$	FWHM	$\xi, X_i$
~0%	10.34	0.82	0.28, 4	11.72	1.12	0.50, 4	11.50	1.25	0.45, 4
20%	12.40	0.54	0.02, 4	13.98	1.24	0.93, 4	14.00	0.97	0.28, 4
~35%	12.41	0.51	0.03, 4	14.97	0.70	0.27, 4	14.11	0.98	0.31, 4
40%	15.28	0.56	0.14, 4	15.02	0.72	0.27, 4	14.83	0.81	0.17, 4
60%	15.56	0.47	0.06, 4	15.25	0.67	0.23, 4	15.44	0.78	0.28, 4
80%	15.75	0.47	0.06, 4	15.43	0.68	0.20, 4	15.82	0.70	0.14, 4

*Note:* Position ( $d(001)$ ) and FWHM of the 001 reflection are given in Å and in  $^{\circ}2\theta$  Cu  $K\alpha$ , respectively. The  $\xi$  parameter which accounts for the departure from rationality of the  $00\ell$  reflection series is calculated as the standard deviation of the  $\ell \times d(00\ell)$  values calculated for the  $X_i$  measurable reflections over the 2-50 $^{\circ}2\theta$  Cu  $K\alpha$  angular range

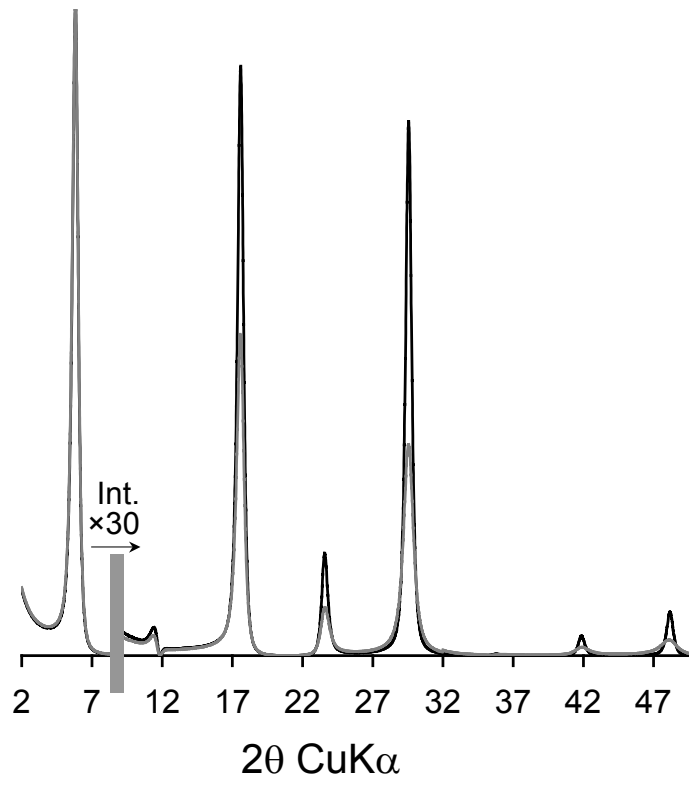
**TABLE 2.** Optimum structural parameters used for the simulation of XRD profiles.

K-SWy						
RH	0	20	room	40	60	80
L. Tck. 2W	-	15.55	15.55	15.55	15.55	15.55
nH <sub>2</sub> O		2×3.2	2×3.2	2×3.2	2×3.2	2×3.2
L. Tck. 1W	12.40	12.42	12.50	12.55	12.60	12.65
nH <sub>2</sub> O	2.0	4.0	4.0	4.0	4.0	4.0
L. Tck. 0W	10.00	10.00	10.00	10.00	10.00	10.00
N	7.5	12.0	11.0	12.0	13.0	9.0
$\sigma^*$	4.0	5.0	5.0	5.0	5.0	5.0
$\sigma_z$	0.25	0.20	0.20	0.20	0.20	0.20
Na-SWy						
RH	0	20	room	40	60	80
L. Tck. 2W	-	15.40	15.45	15.45	15.45	15.45
nH <sub>2</sub> O		2×3.2	2×3.2	2×3.2	2×3.5	2×3.5
L. Tck. 1W	12.30	12.37	12.45	12.46	12.47	12.55
nH <sub>2</sub> O	2.8	3.0	3.3	3.6	3.8	4.5
L. Tck. 0W	9.60	9.60	9.60	9.60	9.60	9.8
N	7.5	9.5	7.5	7.5	7.0	6.5
$\sigma^*$	6.0	5.0	3.2	2.8	3.0	2.8
$\sigma_z$	0.15	0.15	0.22	0.25	0.22	0.17
Li-SWy						
RH	0	20	room	40	60	80
L. Tck. 2W	-	15.50	15.55	15.55	15.55	15.75
nH <sub>2</sub> O		2×2.6	2×2.6	2×2.6	2×2.6	2×3.2
L. Tck. 1W	12.10	12.255	12.265	12.28	12.296	12.40
nH <sub>2</sub> O	2.2	3.7	3.9	3.9	4.2	4.2
L. Tck. 0W	9.60	9.60	9.60	9.60	9.60	9.60
N	7.0	9.5	9.5	9.0	7.8	7.5
$\sigma^*$	10.0	6.0	6.0	6.0	6.0	3.7
$\sigma_z$	0.40	0.23	0.23	0.23	0.23	0.20

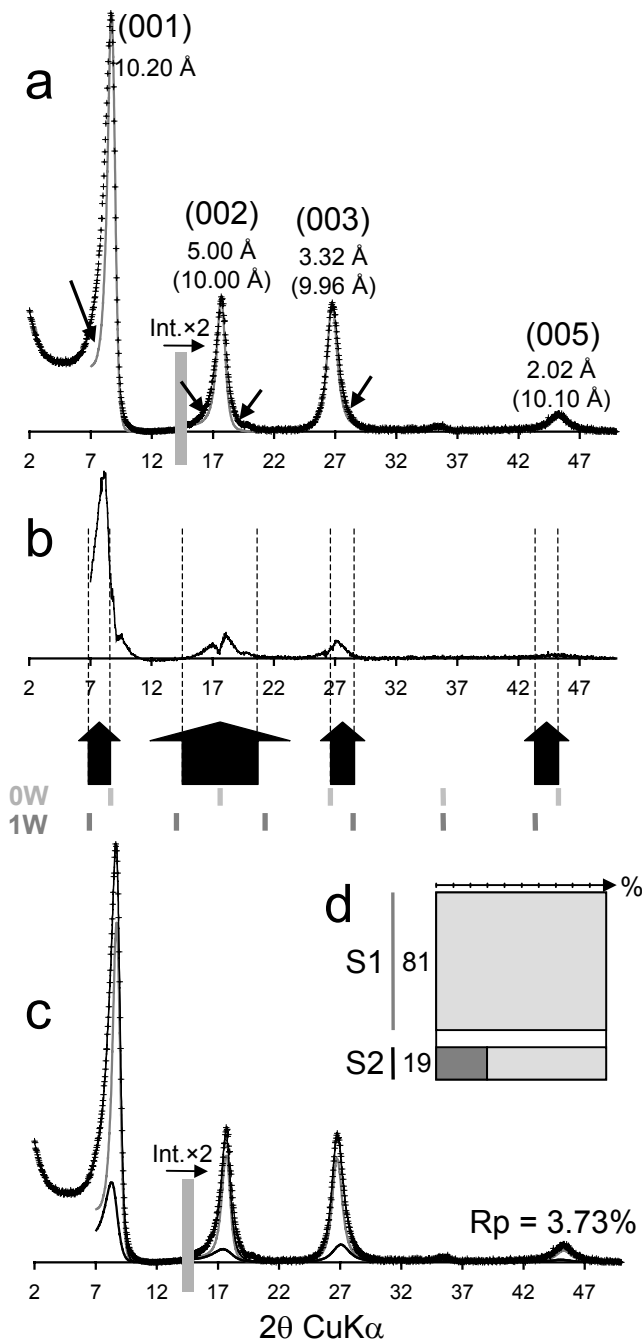
Sr-Swy						
RH	0	20	room	40	60	80
L. Tck. 2W	-	15.10	15.30	15.30	15.53	15.73
nH <sub>2</sub> O		2×2.5	2×3.0	2×3.0	2×3.0	2×3.0
L. Tck. 1W	11.90	12.35	12.35	12.40	12.58	12.70
nH <sub>2</sub> O	2.0	3.0	3.0	3.5	3.5	5.5
L. Tck. 0W	9.80	10.00	10.00	10.00	10.00	10.00
N	11.0	10.0	10.0	9.0	7.5	7.5
$\sigma^*$	10.0	6.0	6.0	5.5	5.5	5.5
$\sigma_z$	0.25	0.25	0.25	0.30	0.35	0.35
Ca-SWy						
RH	0	20	room	40	60	80
L. Tck. 2W	14.30	14.79	15.10	15.11	15.30	15.51
nH <sub>2</sub> O	2×2.5	2×2.6	2×3.3	2×3.3	2×3.3	2×3.3
L. Tck. 1W	11.65	12.58	12.75	12.76	12.80	12.85
nH <sub>2</sub> O	1.5	3.2	3.2	3.2	3.2	3.2
L. Tck. 0W	10.00	10.00	10.00	10.00	10.00	10.00
N	8.0	8.0	8.0	8.0	7.0	6.0
$\sigma^*$	7	11.0	7.0	7.5	7.0	6.5
$\sigma_z$	0.35	0.36	0.27	0.27	0.27	0.27
Mg-Swy						
RH	0	20	room	40	60	80
L. Tck. 2W	13.90	14.20	14.45	14.80	15.42	15.80
nH <sub>2</sub> O	2×1.73	2×1.73	2×1.73	2×3.0	2×3.0	2×3.2
L. Tck. 1W	11.50	12.10	12.30	12.50	12.70	13.00
nH <sub>2</sub> O	2.5	2.5	3.0	3.0	3.5	3.5
L. Tck. 0W	10.00	10.00	10.00	10.00	10.00	10.00
N	8.0	8.0	7.0	6.5	6.5	6.0
$\sigma^*$	9.0	5.5	5.2	5.2	5.2	5.2
$\sigma_z$	0.45	0.45	0.45	0.52	0.52	0.52

*Note:* Layer thickness (L. Tck.) of bi-hydrated, mono-hydrated and dehydrated layers (2W, 1W and 0W layers, respectively) are given in Å. For hydrated layers, the amount of interlayer H<sub>2</sub>O molecules is indicated per O<sub>20</sub>(OH)<sub>4</sub>. N is the mean number of layers in the coherent scattering domain, orientation parameter  $\sigma^*$  and layer thickness variability parameter ( $\sigma_z$ ) are given in ° and in Å, respectively.

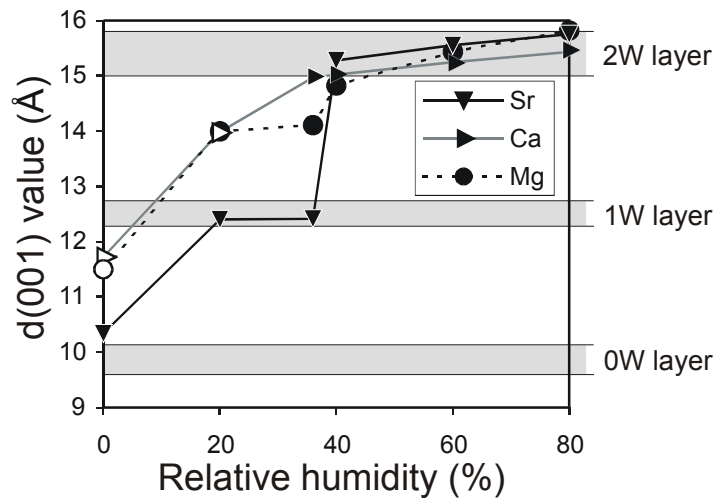
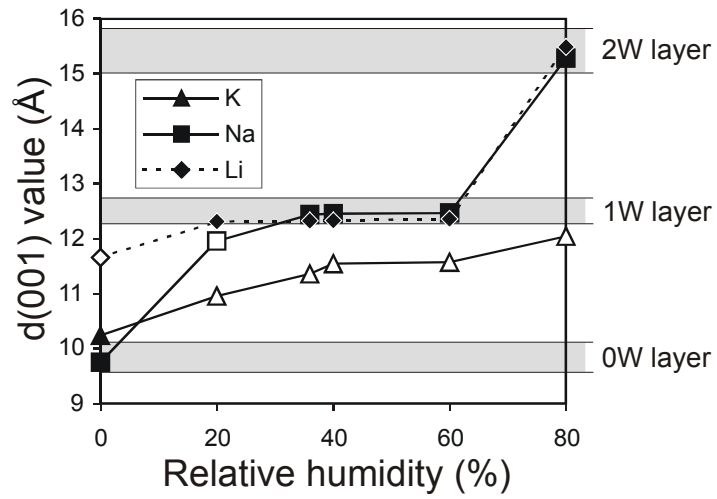




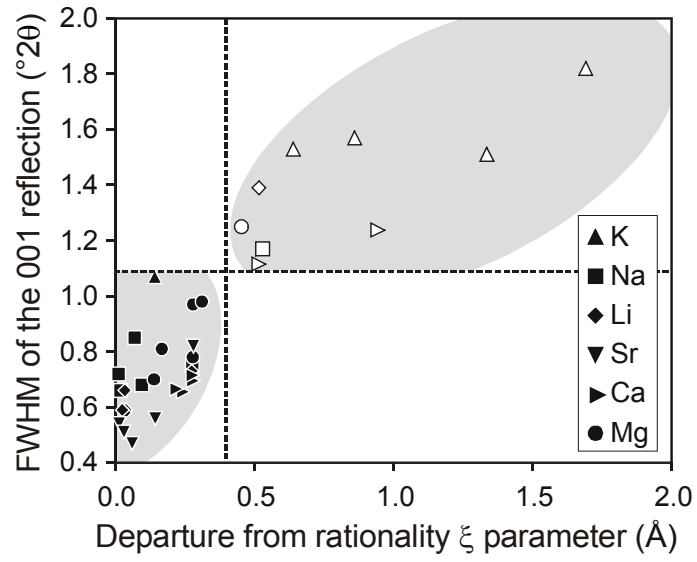
Ms#1776 Ferrage et al. Fig. 01



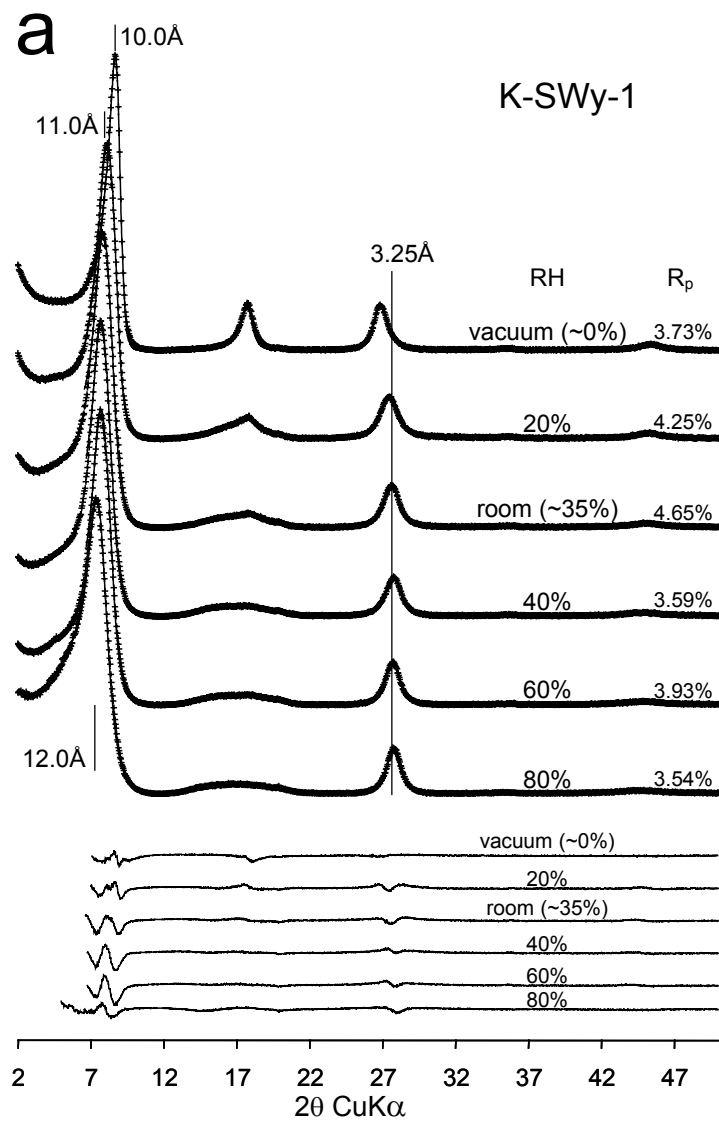
Ms#1776 Ferrage et al. Fig. 02



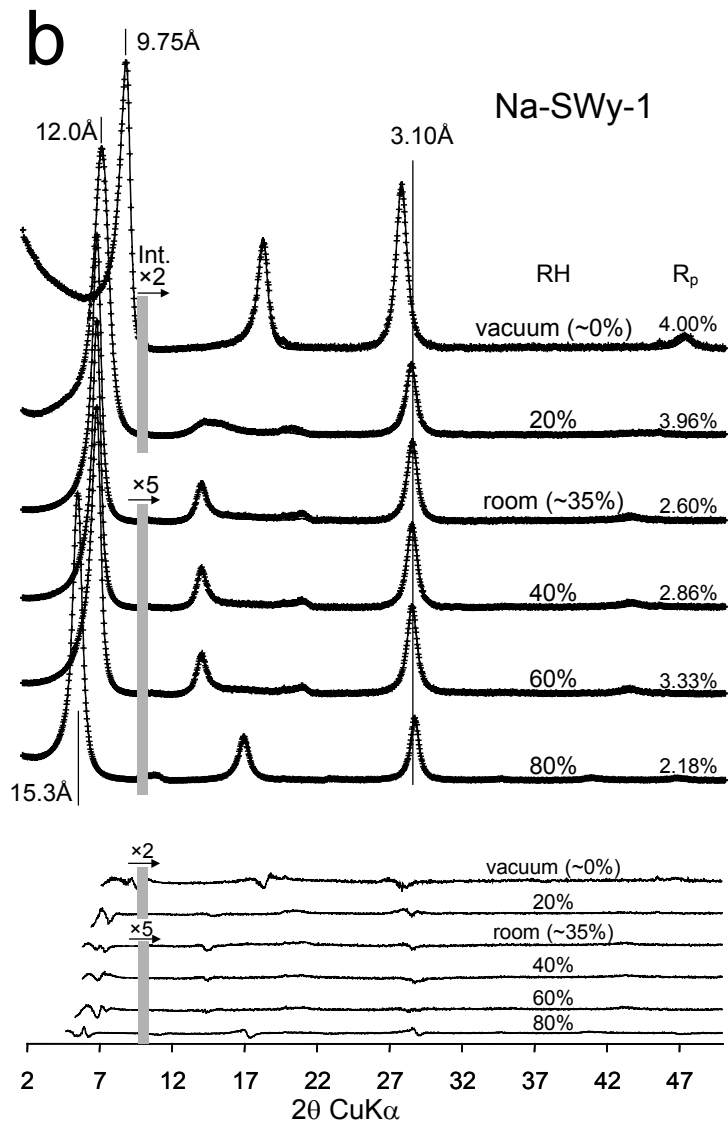
Ms#1776 Ferrage et al. Fig. 03



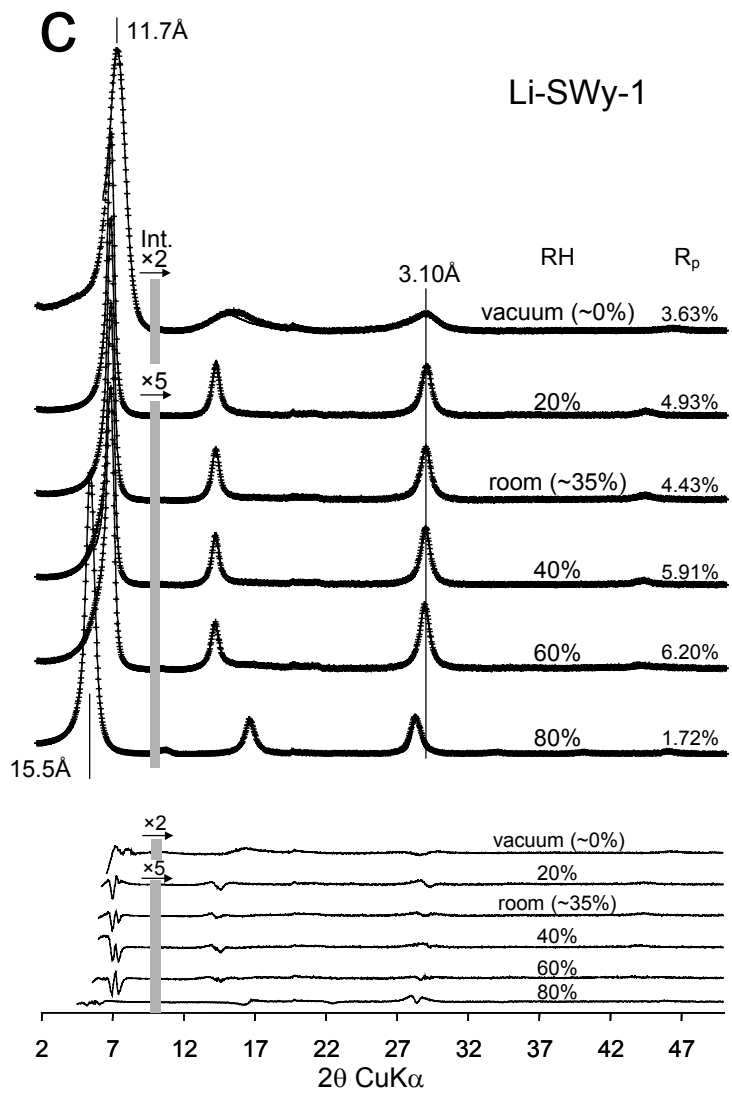
Ms#1776 Ferrage et al. Fig. 04



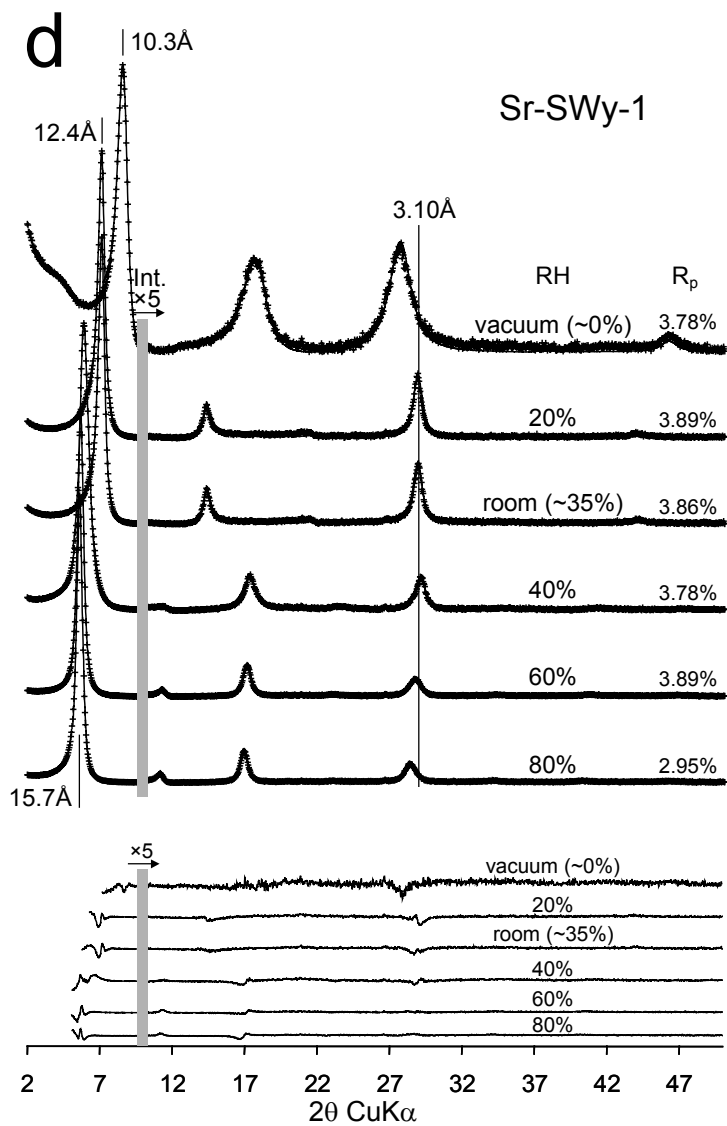
Ms#1776 Ferrage et al. Fig. 05a



Ms#1776 Ferrage et al. Fig. 05b

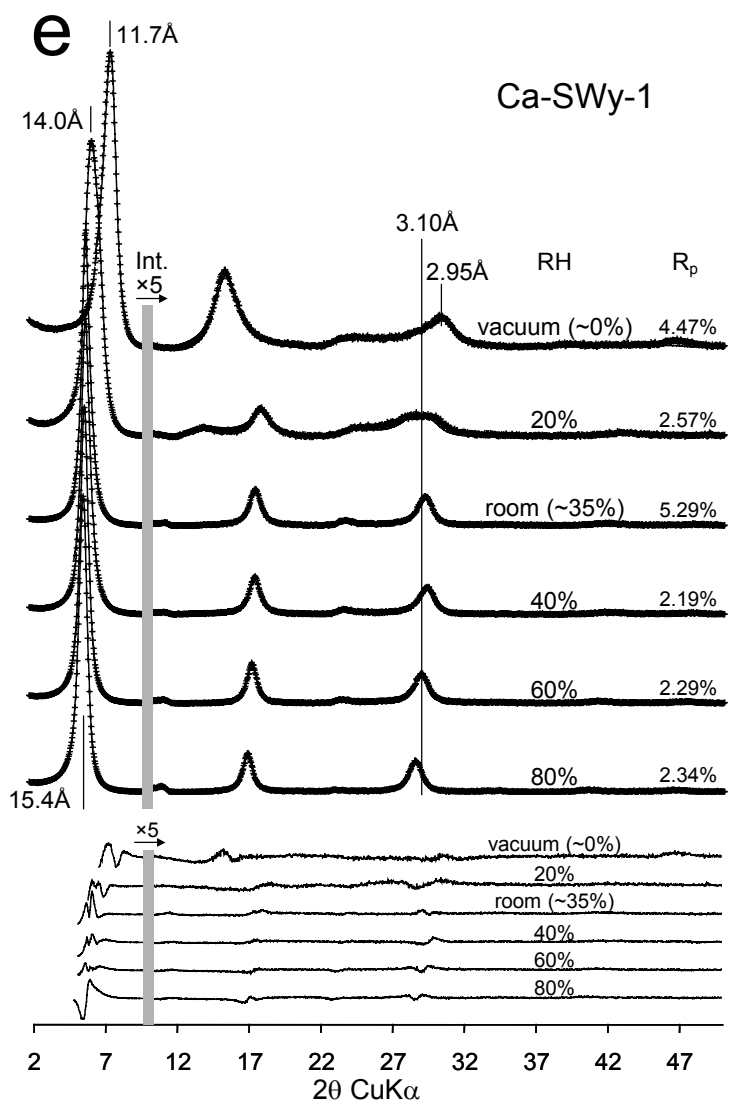


Ms#1776 Ferrage et al. Fig. 05c

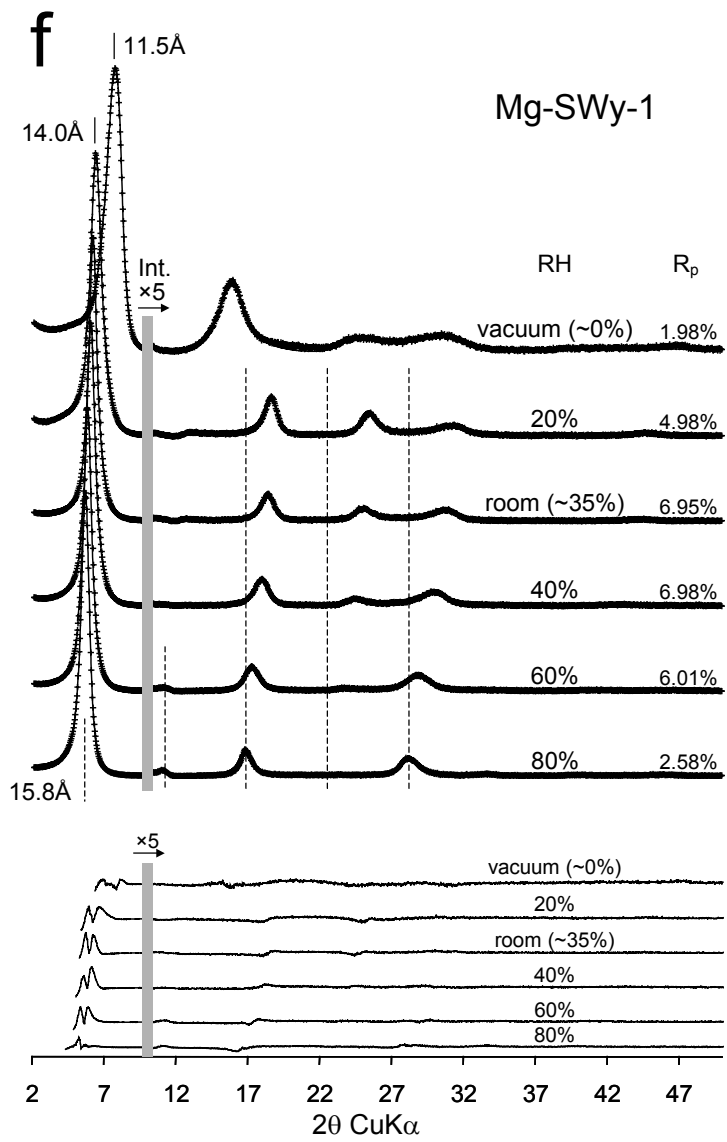


Ms#1776 Ferrage et al. Fig. 05d



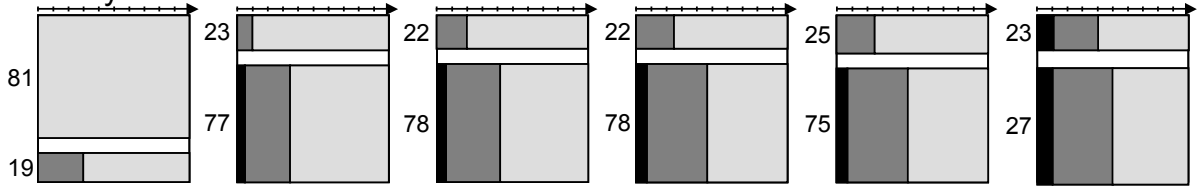


Ms#1776 Ferrage et al. Fig. 05e

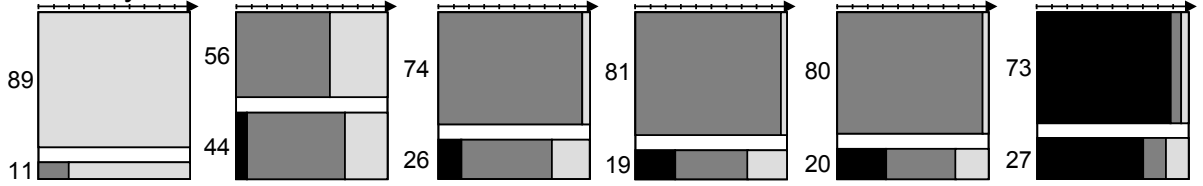


Ms#1776 Ferrage et al. Fig. 05f

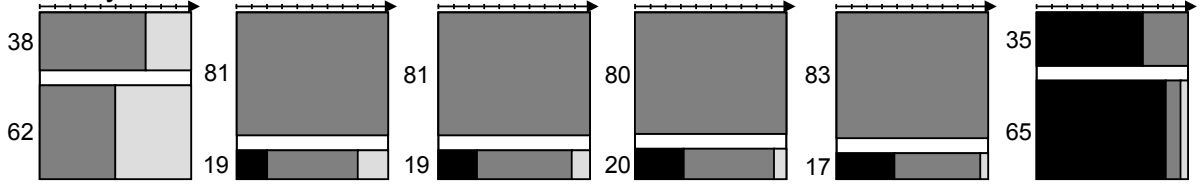
a – K-SWy-1



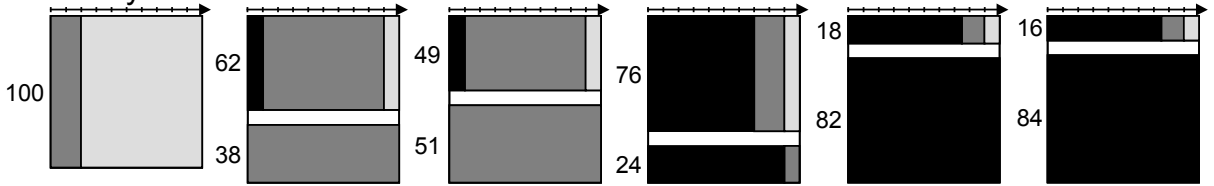
b – Na-SWy-1



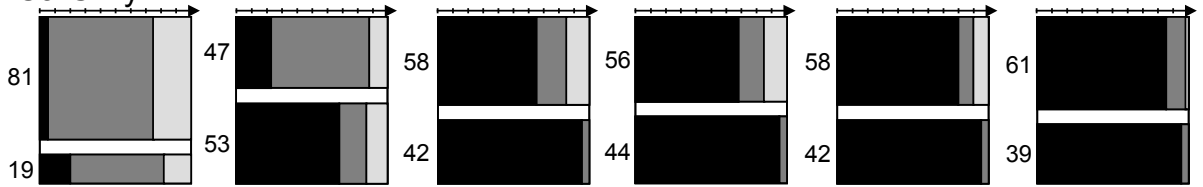
c – Li-SWy-1



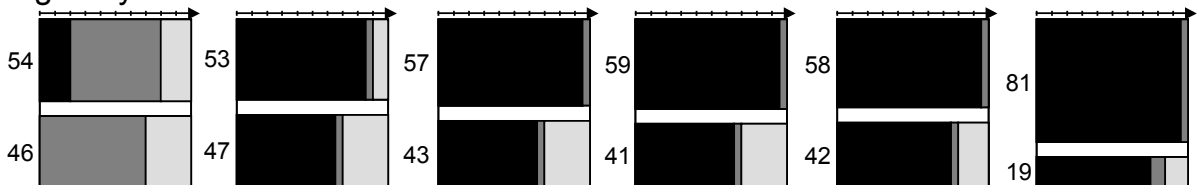
d – Sr-SWy-1



e – Ca-SWy-1



f – Mg-SWy-1



vacuum (~0%)

20%

room (~35%)

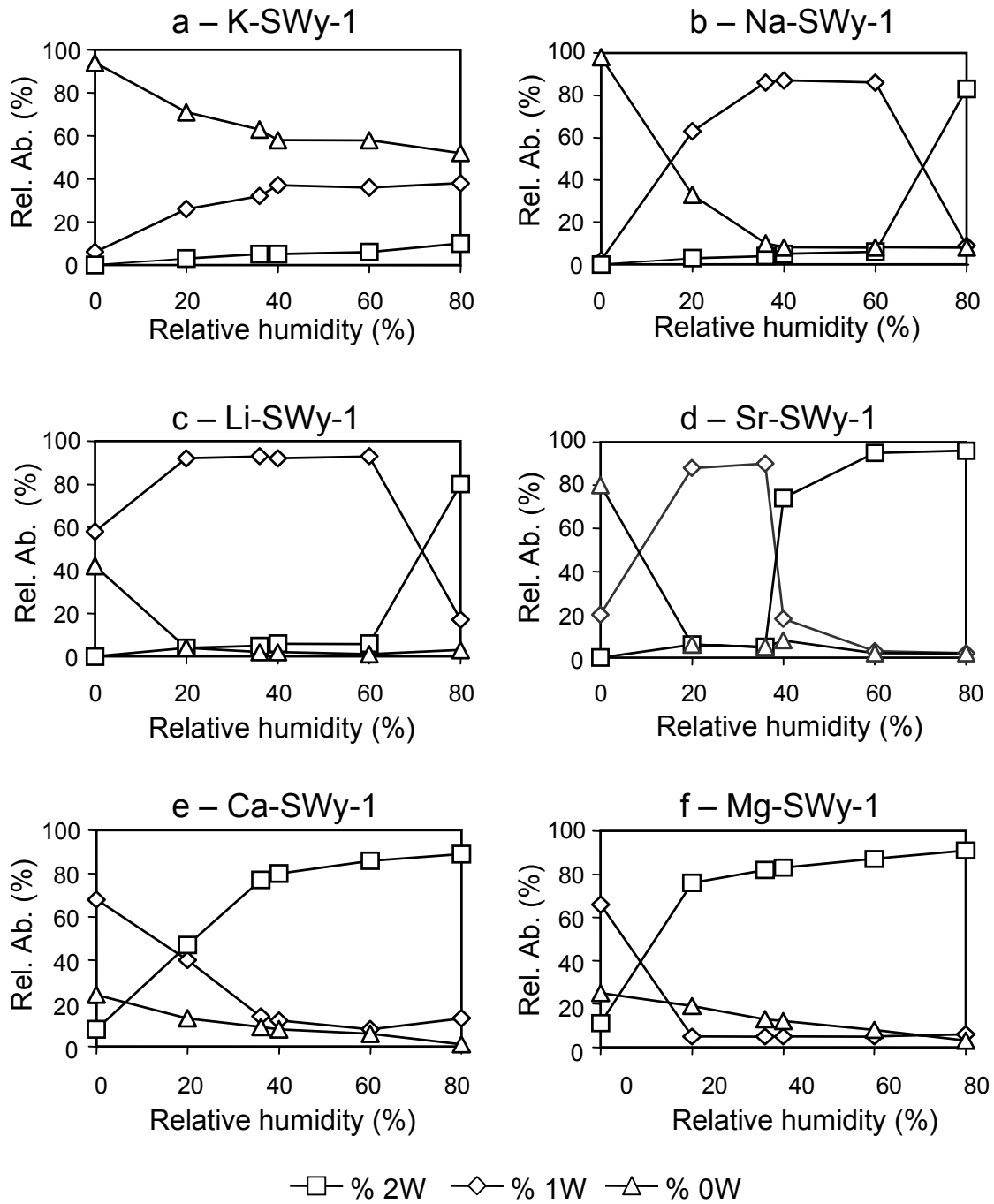
40%

60%

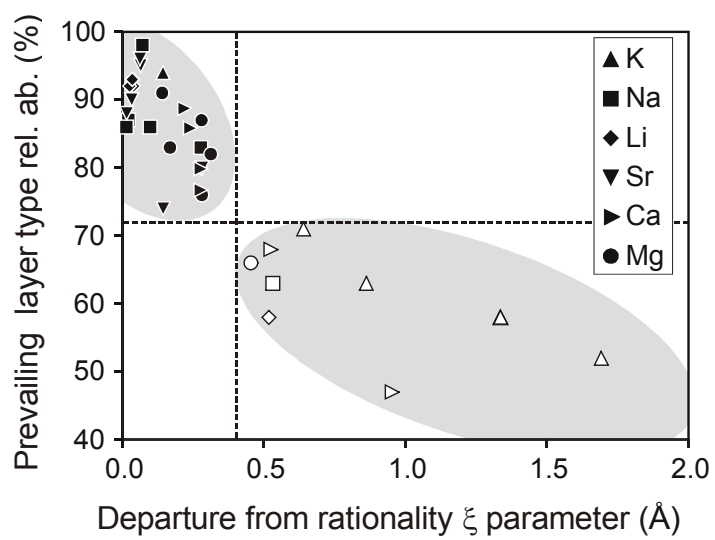
80%

□0W    ■1W    ■2W

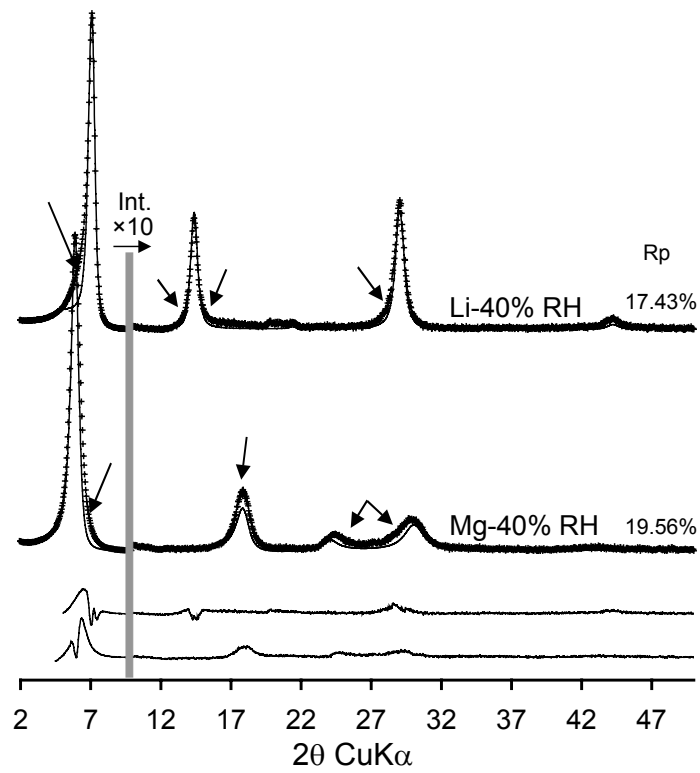
Please print in 2 columns format



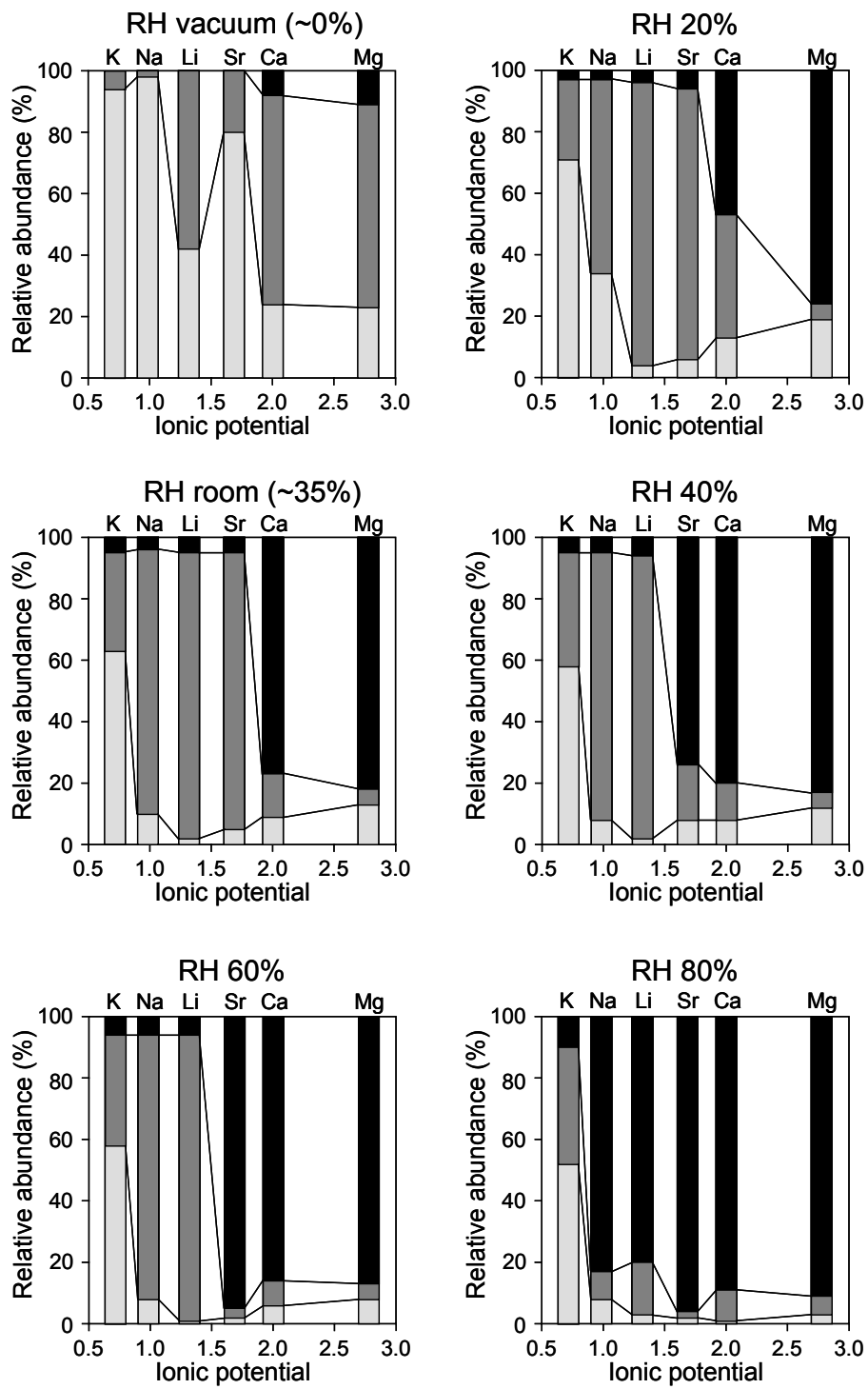
Please print in 2 column format



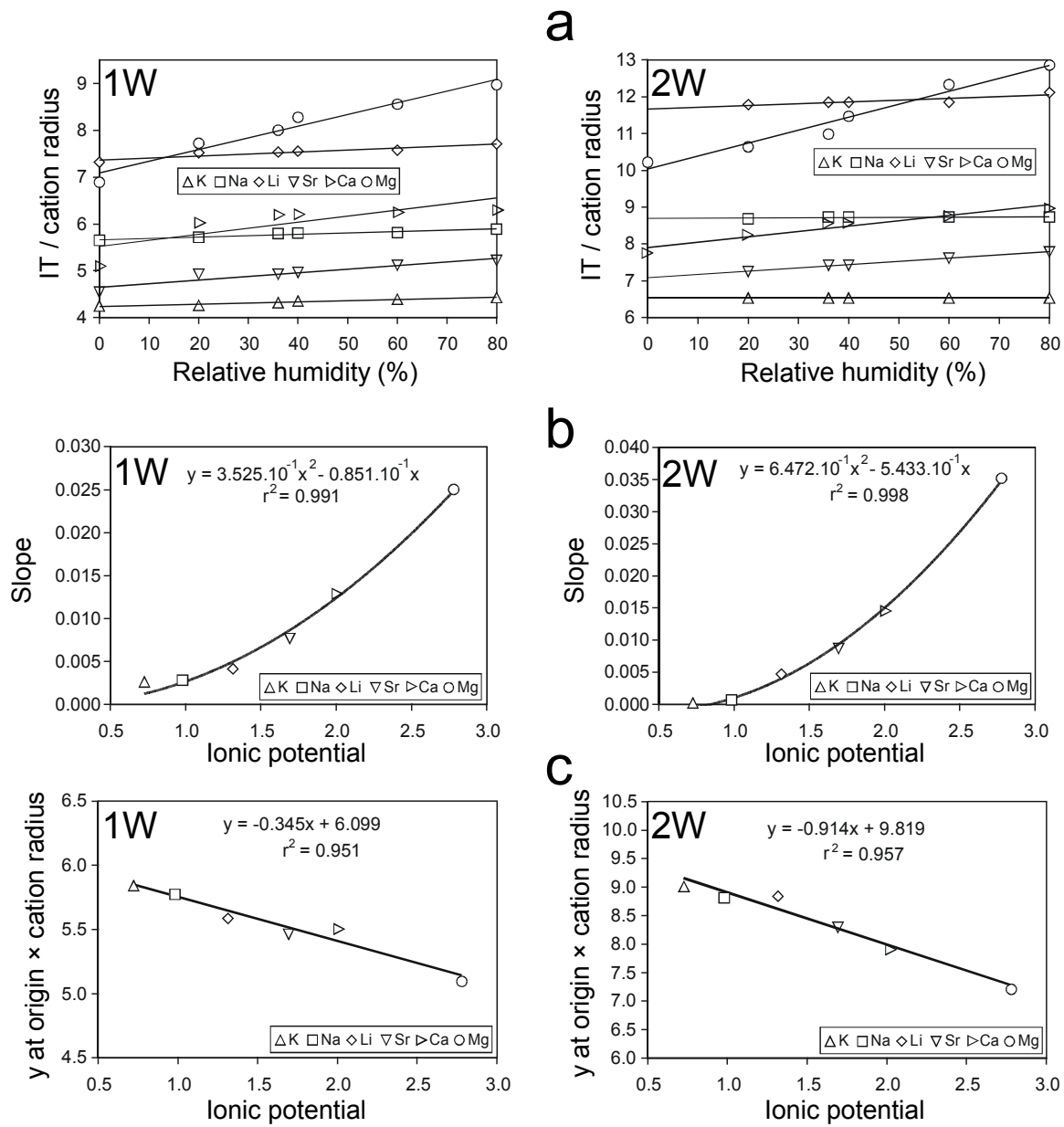
Ms#1776 Ferrage et al. Fig. 08



Ms#1776 Ferrage et al. Fig. 09



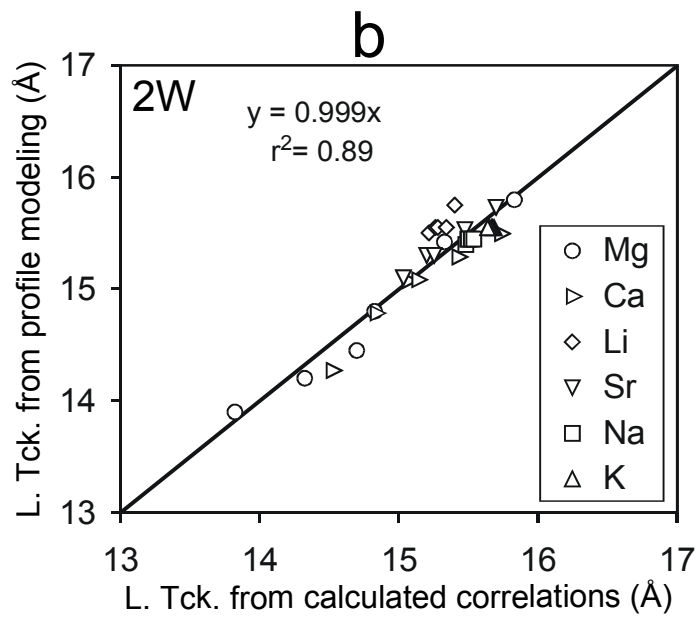
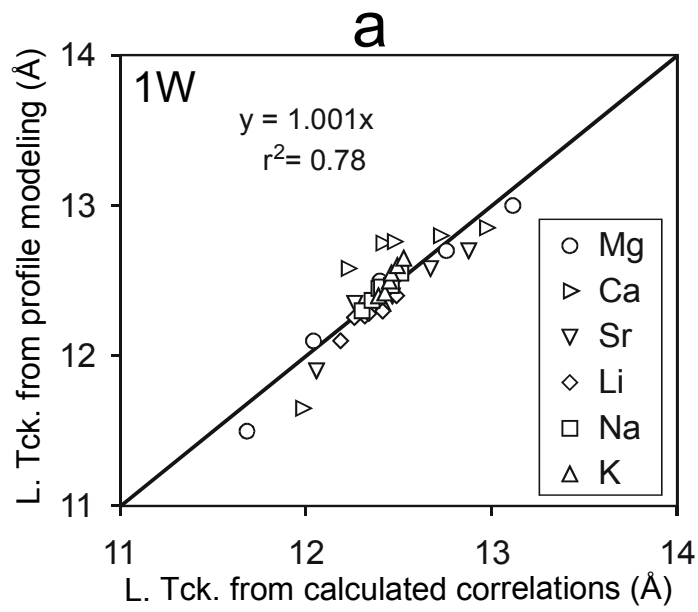
Please print in 2 column format



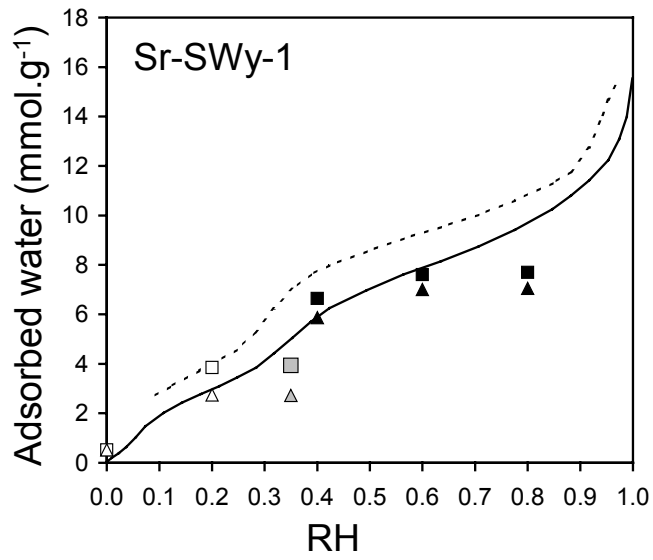
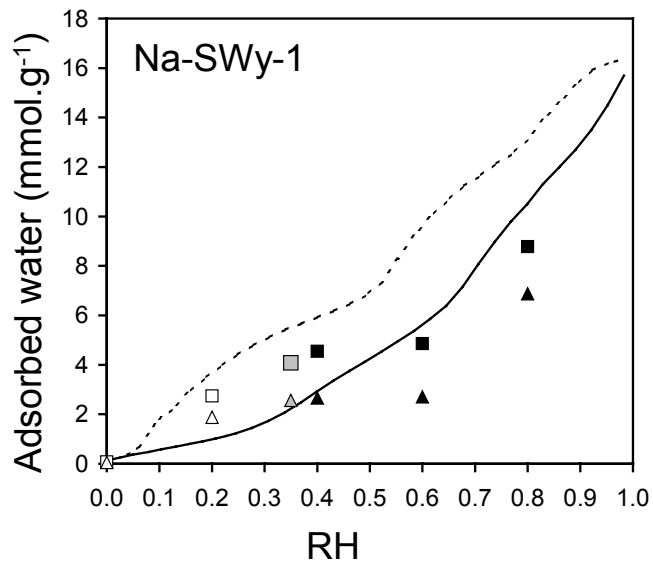
Please print in 2 column format

Ms#1776 Ferrage et al. Fig. 11

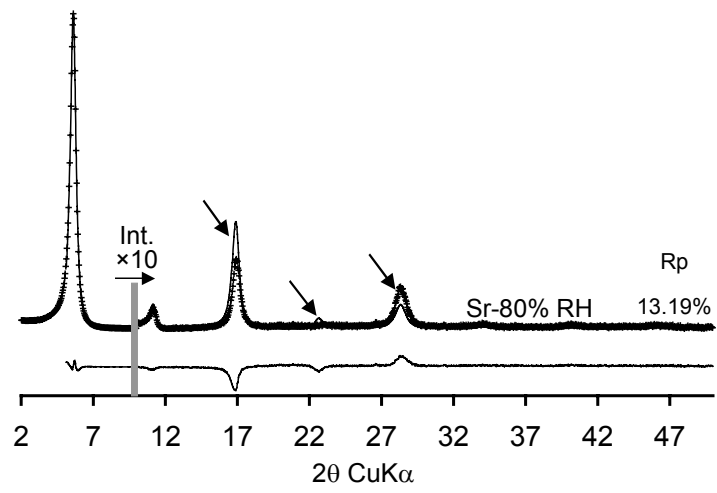




Ms#1776 Ferrage et al. Fig. 12



Ms#1776 Ferrage et al. Fig. 13



Ms#1776 Ferrage et al. Fig. 14